José Miguel Vaz da Cunha

Bachelor in Micro and Nanotechnologies Engineering

Dissertation for obtaining the degree of Master of Science in Micro and Nanotechnologies Engineering

Insulator materials for electrical passivation of thin film solar cells

Supervisor: Doctor Pedro Salomé, Group Leader, International Iberian Nanotechnology Laboratory

Co-supervisor: Doctor Hugo Águas, Auxiliary Professor, Faculty of Sciences and Technology, New University of Lisbon

Examination Committee:

Chairperson: Doctor Luís Pereira

Rapporteurs: Doctor Joana Pinto
Doctor Pedro Salomé

September 2017

Insulator materials for electrical passivation of thin film solar cells
Copyright © José Miguel Vaz da Cunha, Faculdade de Ciências e Tecnologia, Universidade Nova de Lisboa.
A Faculdade de Ciências e Tecnologia e a Universidade Nova de Lisboa têm o direito, perpétuo e sem limites geográficos, de arquivar e publicar esta dissertação através de exemplares impressos reproduzidos em papel ou de forma digital, ou por qualquer outro meio conhecido ou que venha a ser inventado, e de a divulgar através de repositórios científicos e de admitir a sua cópia e distribuição com objetivos educacionais ou de investigação, não comerciais, desde que seja dado crédito ao autor e editor.

“The role of the infinitely small is infinitely large.”
Louis Pasteur

Acknowledgements

I would like to start by acknowledging Prof. Doctor Hugo Águas, my Co-supervisor at FCT for accepting my master thesis request and for all the support during these months. I also want to acknowledge my Supervisor Prof. Doctor Pedro Salomé for everything. There are no enough words to thank everything that you did for me. Since the internship, you taught me things that I never imagined. Not only in the professional way, but also in the personal one. More than a supervisor, you were a really good friend. I will never forget the discussions from I learnt so much. I also want to thank all the members of the INL's NOA group, namely Sourav Bose and Prof. Doctor Paulo Fernandes. Prof. Doctor Paulo with you I learnt considerably about electrical measurements. Without our discussions and your recommendations, I could not achieve the results that I have. With all the meetings, I learnt a great deal about other topics not directly related with my theme. I want to thank everyone in INL that helped me, without them this stage would not be possible, namely Doctor Yury Kolen'ko and Doctor João Gaspar for letting me use their equipment, Doctor Jérôme Borme for having the patience to answer all my questions and Eng. Helder Fonseca for the grateful help in the clean room during the insulator depositions.

A special acknowledgment to Prof. Doctor Rodrigo Martins and Prof. Doctor Elvira Fortunato due to the creation of this course, Micro and Nanotechnologies Engineering, the first one in Portugal. Moreover, by allowing me, during the course, to use the CENIMAT|i3N and CEMOP facilities that they created, making a huge difference between having just theory lessons, and having the theory lessons jointly with practical ones, in those facilities. Every time that I needed something you were here to help. I also want to thank all the professors in the department that always tried to help us not only in the classes but also outside them, namely Prof. Doctor Luís Pereira, Prof. Doctor Rui Igreja, Prof. Doctor Pedro Barquinha, among many others. I want also to thank Prof. Doctor Manuel Mendes and Eng. Tiago Mateus for the aluminium deposition.

I want to thank Prof. Doctor Joaquim and Eng. Jennifer from University of Aveiro/i3N for the measurements and the PL learning. I really am grateful for the discussions about a completely new theme for me that was not easy to learn. I also want to thank Prof. Doctor Bart Vermang and Eng. Siddhartha Garud for the TRPL measurements at IMEC; and Doctor Adam Hultqvist from Uppsala University for the ALD deposition.

Gostava de agradecer a todos os meus colegas do meu curso e da faculdade que me apoiaram ao longo desta longa jornada de cinco anos. A entreajuda foi enorme e sem dúvida que todos contribuíram para a minha aprendizagem. Gostava de agradecer especialmente à Cátia e ao Vasco por todos os bons momentos que passamos, mas também por todas as discussões produtivas. Aprendi imenso com vocês, não só profissionalmente, mas também pessoalmente.

À direção da iNOVAfuture 2016, Cátia, Vasco, Tiago e Pedro foi um ano cheio de descobertas para nós, foi difícil, mas fizemos um excelente trabalho que não teria sido possível sem a vossa motivação e dedicação que tiveram pela causa! Acho que todos crescemos imenso com esta experiência, falo por mim, pois nunca tinha tido tal responsabilidade.

Kateryna Zrazhevska, espero que a nossa amizade dure para a eternidade, ensinaste-me muito, quando tiveste de me dar na cabeça também o soubeste fazer, e sei que sem ti, a faculdade não teria sido a mesma coisa. Admiro-te imenso, admiro a forma como pensas, e abriste-me os olhos para coisas que nunca teria pensado por mim só. Obrigado por tudo!

Durante estes cinco anos estive na melhor residência do país, com as melhores pessoas de sempre. Quem lá passou, sabe que somos uma segunda família, vivendo 24 horas por dia, 7 dias por semana juntos. Não podia deixar de agradecer ao Ricardo Silva por me aturar estes cinco anos! Foi em dúvida uma sorte tremenda ter-te como colega de quarto, sempre serás um grande amigo! Ao restante pessoal: Everton, Baixinho, Nuno Batista, Cláudia, Sabrina, Romero, Catarina Nunes, Bárbara Costa, Raposo, Douglas, Élvio, Dinis, Rafael, Vânia Silva, Inês Rosete muito obrigado, nem sempre foi fácil, mas viver em conjunto tem destas coisas, e foi uma experiencia incrível ter-vos como amigos, sempre me recordarei dos bons momentos que passamos juntos e espero que as aventuras não fiquem por aqui!

Avelino Morganti Neto, não podia esquecer-me de ti, foste mais um grande amigo que fiz na residência, admiro imenso a tua inteligência e criatividade, mas ainda mais a vontade que tens de mudar o mundo, espero que nunca deixes de ser assim porque vais atingir os teus objetivos de certeza! Sabes que um dia irei ao Brasil visitar-te!

Ao meu padrinho Zé Rui e madrinha Sofia Martins por todo o apoio que me deram durante o curso. Sei que posso contar sempre com vocês!

Às minhas afilhadas Maria, Carolina e Bárbara, espero ter ajudado e sido um exemplo para vocês, sabem que poderão sempre contar comigo!

Não podia deixar de agradecer ao caloiro João Barbosa pelos bons momentos que passamos no INL, por ter tido a honra de te ajudar e obviamente aprender contigo. Espero que tenhas um futuro brilhante pela frente!

Por último, mas não menos importante, à minha parceira no crime Márcia e a toda a minha família que sempre estiveram do meu lado desde o inicio desta longa jornada. Sem vocês, não seria o que sou hoje!

Abstract

Currently, renewable energies are being developed in order to replace the fossil fuels. In the renewable energies field, photovoltaics plays a vital role. Thin film technology has the potential to be an important player in the renewable energy market since it can, still decrease significantly its production costs with high material savings while keeping very high values of electrical performance.

One of the thin film technologies is the $Cu(In,Ga)Se_2$ (CIGS). This technology, with long term stability, high values of light to power conversion efficiency is already present in the market but many developments are still needed. One of them deals with the recombination losses happening in the CIGS interfaces which contribute to a decrease in its electrical performance. In order to prevent these losses, passivation layers placed in the interfaces of the CIGS can vastly decrease the recombination losses.

In this work, the aim is to study of the effects of different passivation materials on CIGS technology jointly with the best deposition conditions. Thus, several techniques like Raman spectroscopy, X-ray diffraction and photoluminescence, were used in order to study the CIGS surface damage due to the insulator deposition. Finally, MIS structures were fabricated to study the CIGS-insulator interface electrical properties.

Keywords: CIGS, solar cells, passivation, MIS

Resumo

As energias renováveis estão a ser desenvolvidas de forma a substituir os combustíveis fósseis. Das energias renováveis, a energia fotovoltaica desempenha um papel importante. A tecnologia de filme fino tem o potencial para ser importante, sendo que pode diminuir drasticamente os custos de produção com poupança de material, enquanto mantém altos valores de desempenho elétrico.

Uma das tecnologias de filme fino é o $Cu(In,Ga)Se_2$ (CIGS). Esta tecnologia, com estabilidade de longo prazo e altos valores de eficiência de conversão de energia, já está presente no mercado, mas ainda necessita de inúmeros desenvolvimentos. Um deles está relacionado a recombinação que acontece nas interfaces do CIGS que contribuem para a redução do desempenho elétrico. De forma a prevenir estas perdas, camadas de passivação colocadas nas interfaces do CIGS podem diminuir consideravelmente as perdas por recombinação.

Neste trabalho, o objetivo é o estudo dos efeitos de diferentes materiais de passivação em tecnologia de CIGS juntamente com as melhores condições de deposição. Várias técnicas, nomeadamente espectroscopia de Raman, difração de raio-X e fotoluminescência, foram usadas para o estudo do dano causado à superfície do CIGS devido à deposição do isolante. Finalmente, estruturas MIS foram fabricadas para o estudo das propriedades elétricas da interface CIGS-isolante.

Palavras-chave: CIGS, células solares, passivação, MIS

Contents

Acknowledgements .... **vii**
Abstract .... **ix**
Resumo .... **xi**
Contents .... **xiii**
List of figures .... **xv**
List of tables .... **xvii**
Symbols .... **xix**
Acronyms .... **xxiii**
Motivation and Objectives .... **xxv**
1 Introduction **1**
1.1. Solar cell single-diode model 1
1.2. $Cu(In,Ga)Se_2$ (CIGS) based solar cells 2
1.2.1 Material and advantages *2*
1.2.2 State of the art *3*
1.3. Passivation 3
1.4. MIS structures 4
1.4.1 Fixed insulator charges (Q_f) *4*
1.4.2 Density of interface defects (D_{it}) *5*
2 Materials and methods **7**
2.1. Experimental planning 7
2.2. MIS fabrication and depositions techniques 8
2.3. Characterization techniques 10
2.4. Electrical measurement tool 10
3 Results and Discussion **13**
3.1. Raman spectroscopy 13
3.2. X-ray diffraction 16
3.3. Photoluminescence 17
3.4. Time-resolved photoluminescence 17
3.5. Raman and photoluminescence results overview 18
3.6. Electrical measurements 19
3.6.1 Fixed insulator charges (Q_f) *22*
3.6.2 Density of interface defects (D_{it}) *26*
3.7. Summary 28
4 Conclusion and Future Perspectives **29**
5 Bibliography **31**
6 Annexes **35**
6.1. Annex A – Raman spectra 35
6.2. Annex B – X-ray diffraction spectra 37
6.3. Annex C – Fixed insulator charges (Q_f) and Density of interface defects (D_{it}) 39

List of figures

Figure 1.1 – a) Current-voltage curve characteristics of a solar cell under light. Adapted from [11].; b) One-diode circuit model. 1
Figure 1.2 - State-of-the-art CIGS solar cell structure. The incoming light is reaching the solar cell on top of the shown structure. The layers are not at scale. 2
Figure 1.3 - Typical structure of CIGS chalcopyrite. The indium atoms can be replaced by gallium. Adapted from [16]. 2
Figure 1.4 – i) First diagram of PERC structure [2]. ii) Schematic representation of the rear of (a) a p-type Si solar cell with a surface passivation stack and micron-sized local point contacts and (b) a CIGS solar cell with a surface passivation stack and nano-sized local point contacts. Also, typical base/absorber thickness, minority carrier diffusion length (L_n), contact opening diameter and distance between contact openings are specified [18]. 4
Figure 1.5 - V_{fb} is extrapolated from the linear part of $[(C_{in}/C_m)^2-1](V_G)$ characteristic to the zero value [38]. 5
Figure 1.6 - Equivalent MIS circuits for conductance measurements: a) including interface-trap effect; b) simplified circuit of a); c) device's measured circuit. 5
Figure 2.1 – Experimental planning for the used CIGS pieces. Each CIGS piece was divided into four samples. The CIGS A is to compare different types of depositions mostly with Al_2O_3 (dark blue) and Si_3N_x (light blue). The CIGS B aims to compare the same deposition technique (PECVD) with the same material SiO_x (purple) at different depostion conditions, namely different temperatures and deposition frequencies. A - CdS and B - CdS (red) represent the reference samples for each CIGS piece. The layers are not at scale. 8
Figure 2.2 - HCl etch of CdS and subsequent insulator deposition. The layers are not at scale. 8
Figure 2.3 Mask used in the aluminium thermal evaporation. Holes with three diameters: 1 mm, 2 mm and 3 mm. 9
Figure 2.4 a) Scheme of MIS structure: SLG/Mo/CIGS/insulator/Al. The molybdenum thickness is 350 nm, the CIGS is 2 µm, the insulator 50 nm and the aluminium layer 400 nm (bilayer of 200 nm each). The image is not at scale. b) SEM cross-section of sample A – Al_2O_3 – S........ 9
Figure 2.5 - Measurements of reference and passivated cell: a) C-f curve; b) Mott-Schottky curve and c) N-w curve 11
Figure 3.1 Raman spectra of CIGS A in the left side and CIGS B in the right side. Each curve represents different spots in the same sample: a) A - CdS; b) B - CdS; c) A - Al_2O_3 - S; d) B - SiO_x - 300 ºC; e) A - Si_3N_x; f) B - SiO_x - 150 ºC, HF; g) A - Al_2O_3 - ALD and h) B - SiO_x - 150 ºC, LF........ 14
Figure 3.2 Reference sample's X-ray spectrum of CIGS A with Mo, Al, CdS and $CuInSe_2$ crystalline planes identified........ 16
Figure 3.3 – Photoluminescence spectra of: a) CIGS piece A samples. b) CIGS piece B samples. 17
Figure 3.4 – Minority carriers' lifetime of: a) All samples together including the reference samples; b) Only samples with insulator deposition without the reference samples........ 18
Figure 3.5 - Representative sample with MIS structures having several metal diameters, namely 1 mm, 2 mm and 3 mm. 19
Figure 3.6 – MIS structures using a qualitatively three-degree comparison: good (green), mixed (yellow) and bad (red). CIGS A in the left side and CIGS B in the right side. A) A – CdS; b) A-Al_2O_3 – S; c) B - SiO_x - 300 ºC; d) A - Si_3N_x; e) B - SiO_x - 150 ºC, HF; f) A - Al_2O_3 - ALD; and g) B - SiO_x - 150 ºC, LF........ 21
Figure 3.7 - Shift in C-V curve due to fixed insulator charges in a p-type semiconductor. a) Positive insulator charges effect; b) Negative insulator charges effect. Adapted from [39]. 23
Figure 3.8 - Representative C-V curve. Sample B – SiO_x – 150 ºC, LF. MIS with 2 mm. 24
Figure 3.9 - Representative V_{fb} calculation through the graphical method. Sample B – SiO_x – 150 ºC, LF. MIS with 2 mm. 25

Figure 3.10 - C-V representative curve of sample B – SiO_x – 150 ºC, LF. MIS with 2 mm............... 26
Figure 6.1 Raman spectra with different focus point of CIGS A in the left side and CIGS B in the right side. Each graph represents: a) B – CdS; b) B - SiO_x - 300 ºC; c) A - Si_3N_x - 150 ºC, HF; d) B - SiO_x - 150 ºC, HF; e) A - Al_2O_3 - ALD and f) B - SiO_x - 150 ºC, LF. The curves with low peak intensities are out of focus.. 36
Figure 6.2 Raman spectra of: a) Before CdS removal and b) After CdS removal. 36
Figure 6.3 X-ray diffraction spectra of: a) A - CdS; b) B - CdS; c) A - Al_2O_3 - S; d) B - SiO_x - 300 ºC; e) A - Si_3N_x; f) B - SiO_x - 150 ºC, HF; g) A - Al_2O_3 - ALD; h) B - SiO_x - 150 ºC, LF and i) all samples together. 38
Figure 6.4 - X-ray diffraction spectra zoom of the main CIGS peak (112). a) A - CdS, A - Al_2O_3 - S, A - Si_3N_x and A - Al_2O_3 – ALD samples; b) B - CdS, B - SiO_x - 300 ºC, B - SiO_x - 150 ºC, HF and B - SiO_x - 150 ºC, LF samples. 39
Figure 6.5 - Location of the fixed insulator charges (example of positive charges) and the density of interface defects in the CIGS/insulator interface. Adapted from [40]. 39
Figure 6.6 - Ideal MIS C-V curves of a p-type semiconductor: (a) Low frequency; (b) Intermediate frequency; (c) High frequency; (d) High freequency with fast-sweep (deep depletion). Flat-band voltage of 0V is assumed. Adapted from [40]. 40
Figure 6.7 - Band diagram of a MIS with a p-type semiconductor. a) Ideal MIS in flat-band; b) MIS with positive insulator charges and band bending; c) New flat-band bias. Adapted from [40].... 40

List of tables

Table 1 – Sample's names used hereafter, considering the deposition used and the respective CIGS piece. 7
Table 2 - Representative experimental planning of the AUTOLAB system and LCR comparisons. 12
Table 3 - Comparison between Raman spectroscopy and Photoluminescence measurements using a qualitatively three-degree comparison: good, mixed and bad. 19
Table 4 - Comparison between the samples, taking into account the metal diameter using the percentage of non-shunted structures and qualitatively three-degree overall comparison: good (green), mixed (yellow) and bad (red). 22
Table 5 – C_{in} average and standard deviation values of each diameter for each sample. 24
Table 6 – V_{fb} average and standard deviation values of each diameter for each sample. 25
Table 7 – Q_f values taking into account the average C_{in} and V_{fb} calculated before. The red samples have negative charges in the insulator. 25
Table 8 - D_{it} average and standard deviation values of each diameter for each sample. 27
Table 9 - Summary of all used techniques. Qualitatively three-degree overall comparison: good, mixed and bad. The Q_f measurement has different colours due to not be possible to do a qualitatively comparison. 28

Symbols

Symbol	Name	Unit
A	Area	cm^2
Al	Aluminium	
Al_2O_x/Al_2O_3	Aluminium oxide	
$a\text{-}Si$	Amorphous Silicon	
C	Capacitance	F
CdS	Cadmium Sulphide	
$CdTe$	Cadmium Telluride	
C_{fb}	Flat-band capacitance	F
C_{in}	Insulator capacitance	F
C_{it}	Interface-trap capacitance	F
C_m	Measured capacitance	F
C_p	Frequency-dependent capacitance	F
C_s	Semiconductor capacitance	F
Cu	Copper	
D_{it}	Density of interface defects	$eV^{-1}cm^{-2}$
E_C	Conduction band	eV
E_F	Fermi level	eV
E_g	Energy bandgap	eV
E_V	Valence band	eV
f	frequency	Hz
FF	Fill factor	%
G	Conductance	S
Ga	Gallium	
$GaAs$	Gallium Arsenide	
G_m	Measured conductance	S
G_p	Frequency-dependent conductance	S
H_2O	Hydrogen oxide	
H_2Se	Hydrogen selenide	
HCl	Hydrochloric acid	
HfO_2	Hafnium dioxide	
In	Indium	
J	Current density	A/m^2
J_0	Saturation current density	A/m^2
J_M	Maximum current density	A/m^2
J_{sc}	Short-circuit current density	A/m^2
k	Boltzmann’s constant	J/K

L_n	carrier diffusion length	µm
Mo	Molybdenum	
mpp	Maximum power point	W
n	Ideality factor	%
N	Net acceptors concentration	cm^{-3}
N_2	Nitrogen	
N_2O	Nitrous oxide	
NH_3	Ammonia	
Ni	Nickel	
P_{inc}	Incident power	W
q	Elementary charge	C
Q_f	Fixed insulator charges	cm^{-2}
Q_m	Mobile ionic charges	cm^{-2}
Q_{ot}	Insulator trapped charges	cm^{-2}
R	Resistance	Ω
R_{it}	Interface-trap resistance	Ω
R_s	Series resistance	$Ω/cm^2$
R_{sh}	Parallel resistance	$Ω/cm^2$
Se	Selenium	
Si	Silicon	
Si_3N_x/Si_3N_4	Silicon nitride	
SiH_{4-5}	Silane	
SiO_x/SiO_2	Silicon oxide	
T	Temperature	K
TiO_2	Titanium oxide	
V	Voltage	V
V_{bias}	Supply voltage	V
V_D	Applied voltage across the diode	V
V_{fb}	Flat-band voltage	V
V_G	Applied voltage	V
V_M	Maximum voltage	V
V_{oc}	Open-circuit voltage	V
V_{RMS}	Root mean square voltage	V
w	Distance from interface	nm
X	Reactance	Ω
X_c	Capacitive reactance	Ω
Z	Impedance	Ω
Z'	Impedance real part	Ω

Z''	Impedance imaginary part	Ω
ZnO	Zinc oxide	
$ZnO:Al$	Aluminium doped zinc oxide	
ZnS	Zinc sulphide	
ΔV	Voltage shift	V
η	Power conversion efficiency	%
τ_{it}	Interface-trap lifetime	s
φ_{MS}	Metal-semiconductor work function difference	V
ω	Angular frequency	rad/s

Acronyms

ALD	Atomic layer deposition
CGS	Copper Gallium Selenide
CIGS	Copper Indium Gallium Diselenide, $Cu(In,Ga)Se_2$
CIS	Copper Indium Selenide
CPE	Constant Phase Element
CVD	Chemical vapour deposition
DC	Direct current
HF	High frequency
INL	International Iberian Nanotechnology Laboratory
i-ZnO	intrinsic Zinc oxide
LF	Low frequency
MIS	Metal-Insulator-Semiconductor
OVC	Ordered Vacancy Compound
PECVD	Plasma-enhanced chemical vapour deposition
PERC	Passivated emitter and rear cell
PL	Photoluminescence
RF	Radio frequency
SEM	Scanning electron microscopy
SLG	Soda-lime-glass
TMA	Trimethyl aluminium
TRPL	Time-resolved photoluminescence
XRD	X-ray diffraction
YAG	Yttrium Aluminium Garnet
ZSW	Center for Solar Energy and Hydrogen Research Baden-Württemberg

Motivation and Objectives

For some time now, burning fossil fuels has been humanity's main source of energy. Nonetheless, the environmental and limited availability issues related to this kind of source are pushing humanity to use other types of energy sources, such as the renewable ones. Environmental friendly technologies have the potential to provide long-term energy solutions together with a sustainable future. One of these technologies is photovoltaics. Taking into account that the sun is, in practical turns, an "unlimited" source, humanity should take the maximum possible advantage of this technology. Photovoltaics are based on the conversion of solar radiation, i.e. photons, into an electrical current that can be used externally. The power conversion efficiency of a solar cell is defined as the ratio of electrical power delivered to the solar power, via light, reaching the solar cell [1]. In order for photovoltaics to be mass deployed at a world-wide level, the solar modules production cost should lower, whereas the electrical performance has to increase [2]. Photovoltaics technology has so much potential, that if the whole global electricity demand would be covered exclusively by solar modules, the total land area needed for light collection would only be approximately 360 000 km^2 of desert area, the equivalent of slightly more than 1 % of Sahara Desert [3,4].

Currently, a considerable amount of research on solar cells is being performed in order to: i) decrease the amount of material usage; ii) increase the solar cells electrical performance. Thin film solar cells are the most proficient technology to increase the electrical performance with high electricity generation at competitive costs while at the same time preserving resources for future generations due to its high electrical performance and low-material usage [5]. Presently, three major thin film technologies are commercialized: amorphous silicon (a-Si), cadmium telluride (CdTe) and $Cu(In,Ga)Se_2$ (CIGS) with world-record power conversion efficiency values of 14 %, 22.1 % and 22.8 % respectively [6,7]. Although the CIGS laboratory cells have higher values of power conversion efficiency than multi-crystalline Si (21.3 %), CIGS modules have power conversion efficiency values of 19.2 %, a value lower than the one of multi-crystalline modules which is currently at 19.9 % [6]. However, the silicon solar cells production cost per Watt is higher than CIGS and with the power conversion efficiency values of CIGS increasing, the costs continues to drop at a faster pace than the one of silicon [8]. Hence, it is predictable that in the near future, CIGS solar cells will be even more vastly used at a world-wide level.

The recombination losses at the CIGS solar cell interfaces are one of the most currently studied issues since by reducing these losses, the solar cell electrical performance can further improve. An innovative solution is to use a passivation layer made of an insulator placed at the interfaces to reduce the recombination losses, hence increasing the electrical performance. This action, was one of the breakthrough discoveries that was done in silicon and that still is to be done in CIGS technology [2].

Due to the importance of developing passivation layers for CIGS technology, the work developed in this thesis is focused on the study of the effects of the passivation material and on the best deposition conditions to be used as a passivation layer. Insulator layers, such as, SiO_2, Al_2O_3 and Si_3N_4, were tested as the passivation material. Several characterization techniques were performed in order to allow us to identify which deposition conditions are capable of optimizing the passivation effects on the CIGS absorber while maintaining the CIGS surface as pristine as possible. Raman scattering and X-ray diffraction were used for the study of the possible CIGS damage due to the insulator deposition. Metal-Insulator-Semiconductor (MIS) structures were made on CIGS absorber layers with aluminium as the top metal contact for electrical testing. The main thesis objective is the identification of the key parameters that will allow to choose an insulator material among several candidates capable of passivating the CIGS interfaces.

1 Introduction

1.1. Solar cell single-diode model

The current density-voltage (J-V) curve, presented in **Figure 1.1 a)**, is one of the most important features of solar cells. Moreover, under light conditions and using the correct model, it is possible to extract figures of merit characteristic of solar cells, being the most important ones the short-circuit current density (J_{sc}), the open-circuit voltage (V_{oc}) and the fill factor (FF), which in turn are used to estimate the power conversion efficiency (η) of a solar cell device, defined by [9]:

$$\eta = \frac{J_M V_M}{P_{inc}} = \frac{J_{SC} V_{OC} FF}{P_{inc}} \quad (1)$$

where J_M is the maximum current density, V_M is the maximum voltage and P_{inc} is the incident power.

In **Figure 1.1 a)**, R_{sh} is the parallel resistance and R_s is the series resistance. It is also shown how some of the solar cells figures of merit are extracted: V_{oc} corresponds to the value of the voltage when the current density is equal to zero, J_{sc} is the value of current density when the voltage is zero, the fill factor (*FF*) is the ratio between the maximum generated power divided by $J_{sc} \times V_{oc}$. The maximum power point (*mpp*), is the maximum voltage V_M in **Figure 1.1 a)**, (compared to V_{oc}) multiplied by the maximum current density J_M in **Figure 1.1 a)**, (compared to J_{sc}) [10].

There are several models to electrically represent a solar cell. In CIGS solar cells the most used one is the “single-diode model” represented in **Figure 1.1 b)** [12].

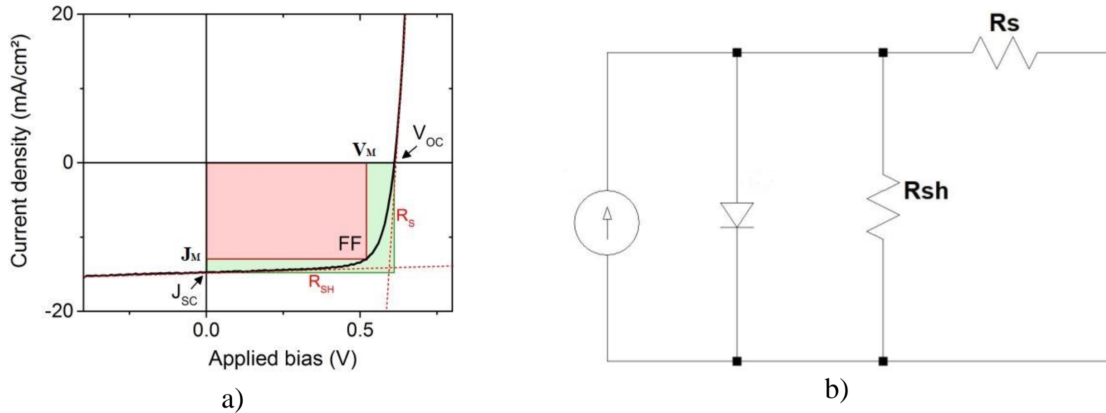

a) b)

Figure 1.1 – a) Current-voltage curve characteristics of a solar cell under light. Adapted from [11].; b) One-diode circuit model.

A single junction solar cell is a device based on a p-n junction, behaving in the same way as a diode. The typical equation describing this model, is [9,13]:

$$J = j_0 \left[\exp\left(\frac{qV_D}{nkT}\right) - 1\right] \quad (2)$$

Where J is the current density, j_0 the saturation current density, q the elementary charge, V_D the applied voltage across the diode, n the the ideality factor for a diode, k the Boltzmann’s constant and T the temperature. In a more realistic way, the cell should be presented with losses taking into account the series resistance and the parallel resistance (or shunt resistance as it is shown in **Figure 1.1 b)**), mathematically defined by:

$$J = j_0 \left[\exp\left(\frac{qV_D - qjR_S}{nkT}\right) - 1\right] + \frac{V_D - jR_S}{R_{sh}} \quad (3)$$

1.2. $Cu(In,Ga)Se_2$ (CIGS) based solar cells

The conventional CIGS solar cell structure is shown in **Figure 1.2**. The solar cell is constituted by the following layers (from bottom to top):

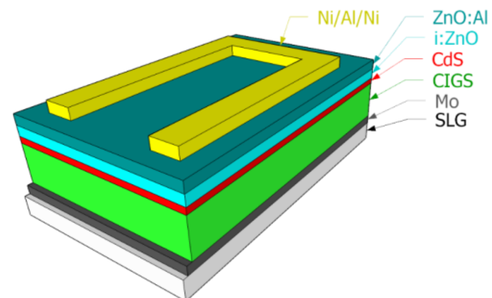

Figure 1.2 - State-of-the-art CIGS solar cell structure. The incoming light is reaching the solar cell on top of the shown structure. The layers are not at scale.

- SLG (soda-lime-glass) substrate as the mechanical support of the entire cell structure. It is generally used due to the fact that it is cheap, roughly planar and it is widely available in several sizes. Its sodium content is beneficial for the CIGS electrical performance, diffusing into the CIGS layer through the molybdenum layer [14].
- Molybdenum (Mo) bilayer as the rear electrical contact. One layer to form a good adhesion with the SLG and the other to form an ohmic contact with the CIGS layer while keeping a high value of electrical conductivity.
- $Cu(In,Ga)Se_2$ (CIGS), a p-type semiconductor, as the absorber layer, being discussed later.
- CdS, a n-type semiconductor, with a direct bandgap of 2.4-2.5 eV, buffer layer that should be able to: i) transmit most of the incoming light; ii) form a high-quality p-n heterojunction including a good energy band alignment match-up [15]; and, iii) to achieve low interface recombination losses.
- Window bilayer. The first, consisting of a very thin layer, below 100 nm, transparent conductive oxide, intrinsic ZnO (i-ZnO) as the interface of the window and buffer layer, creating a favourable band alignment, low interfacial losses and high resistance (preventing conductive paths from the back contact). The second layer, a doped ZnO:Al layer with low resistance, high conductivity and allowing the transmission of the incoming radiation.
- Top contact made of Ni/Al/Ni.

1.2.1 *Material and advantages*

The CIGS compound belongs to the group of the chalcogenides solar cells. The chalcogenides, refers to all chemical compounds with at least one chalcogen anion from the group 16 of the period table (group IV). This anion, in the CIGS case, refers to Se (selenium). One of the chalcogenides groups, are the chalcopyrite solar cells. All chalcopyrites have tetragonal crystal structures as it is shown in **Figure 1.3.**

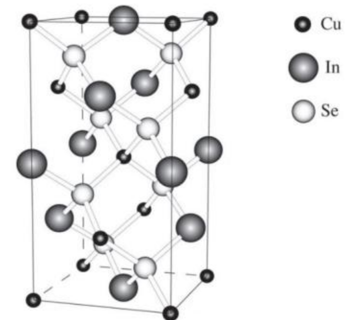

Figure 1.3 - Typical structure of CIGS chalcopyrite. The indium atoms can be replaced by gallium. Adapted from [16].

The chalcopyrites, many of them semiconductors, consists of elements of groups I, III and IV, being also called I-III-IV semiconductors or ternary semiconductors. One of the chalcopyrites used for solar cells is a compound consisting of a solid mixture of copper indium diselenide ($CuInSe_2$, CIS) and copper gallium diselenide ($CuGaSe_2$, CGS). This compound is the copper indium gallium diselenide [$Cu(In_xGa_{1-x})Se_2$, CIGS], where x can vary between 0 and 1.

The CIGS compound is a p-type and direct bandgap semiconductor, with an excellent long-term stability [17]. It has high absorption coefficient values, up to 10^5 cm^{-1}. The high absorption coefficient values are a huge advantage comparing to other solar cells absorbers, like crystalline silicon with an indirect energy bandgap and an absorption coefficient of 10^3 cm^{-1}. This means that the silicon solar cells must be thicker, around 200 µm, whereas CIGS solar cells only need a few micrometres (1-3 µm) for absorbing the same amount of the incoming light with energy values above the bandgap energy. The electron diffusion length is low but in the order of the used thicknesses, from 0.75 µm to 1.5 µm [18] which is a value of importance for the passivation layer.

Another interesting CIGS compound feature is its self-doping nature. This self-doping nature and the p-type property is directly related with Cu vacancies [19].

The properties of the CIGS compound are determined mostly by its Cu content: with low copper concentration (Cu-poor CIGS), which is defined by [Cu]/([Ga]+[In]) < 1, in other words, the concentration of copper is lower than Ga and In together. On the other hand, higher copper concentration (Cu-rich CIGS), defined by [Cu]/([Ga]+[In]) > 1. Cu-rich CIGS has good crystalline properties (big grains), nonetheless its electrical performance is weaker due to lower levels of p-type doping and increased appearance of secondary phases of $Cu_{2-x}Se$. On the other hand, Cu-poor CIGS has poor crystalline properties, but better electrical performance, being preferential for solar cells [9,20].

Another of the CIGS advantages is the possibility to engineer the bandgap and to create a quasi-electric field, by adjusting the amount of gallium content, i.e. by the elemental substitution of In by Ga, making the energy bandgap mutable from 1.02 eV to 1.69 eV.

1.2.2 State of the art

The Shockley–Queisser limit of power conversion efficiency, i.e. the theoretical limit, for the CIGS solar cells is around 33 %, making them one of the most studied solar cells at the present time [1].

The history of CIGS started in 1975, when Bell laboratories scientists achieved a power conversion efficiency of 12 % with CdS on top of $CuInSe_2$ crystals [21,22]. Furthermore, different types of depositions processes (co-evaporation where Cu, In and Se are deposited individually; deposition-reaction process using Cu and In as metallic precursors together with H_2Se) were developed to explore the best deposition method in terms of electrical performance and industrialization [22]. In 1994, National Renewable Energy Laboratories (NREL) invented the so called three-stage process [23]. The three-stage process, was so successful, providing the basis for the solar cells with power conversion efficiency values above 20 % that is still the most used deposition process for laboratory solar cells.

Research teams have been studying alkali elements effects on the absorber layer since the 1980s with Boeing Aerospace Company being the first [24]. Currently, alkali elements effects on CIGS, is a continuous research topic [14]. Similarly, by 1980, B.J. Stanbery and co-workers implemented monolithic integration in the solar-cell stack for module production [24,25]. Another achievement for the CIGS solar cells, was the discovery of the bandgap tuning with the Ga grading. The full comprehension of all the defects in the CIGS absorber layer, how they affect the performance of the solar cell and the solution for those problems is yet not entirely understood. Nevertheless, nowadays the record CIGS solar cell belongs to ZSW with power conversion efficiency of 22.8 % [7]. These solar cells were made in a state-of-the-art laboratory using the co-evaporation method. It is believed that with improvements in interface passivation this efficiency can be largely increased in the next few years [26,27].

1.3. Passivation

The major electrical losses in CIGS solar cells, nowadays, are bulk and interface recombination, which makes them the main performance drawbacks [26].

The common method to reduce the rear surface recombination in state-of-the-art solar cells is by Ga grading [28]. Such grading creates a quasi-electric field that repels the minority carriers from the rear surface [29]. However, the Ga gradient method has several disadvantages. A too low [Ga]/([Ga]+[In]) ratio leads to unsuited band alignment and a to high ratio leads to an increase in the CIGS defect density [11]. With an increase in material grading, potential fluctuations also increase, which decreases the solar cell electrical performance [30].

The interface recombination can be largely supressed by passivating the interfaces. Two types of passivation can be defined: i) chemical passivation, happening when the density of active defects is effectively reduced in the CIGS surface; and ii) field-effect passivation (coulomb repulsion), when the charges inside the passivation layer creates a field effect that repel the carries or enhance the surface inversion (positive charges). When the passivation occurs in the rear interface, another type of effect can happen, an optical effect, which consists in reflecting the light from the passivation layer, thus increasing the path light inside the absorber layer [31]. The use of a passivation layer, jointly with nano-

sized point contacts, is also important to decrease even more the CIGS absorber layer thickness from few micrometres to hundreds of nanometres [18,29].

The idea of nano-sized local point contacts came from silicon solar cells, where this kind of structure is used to increase the V_{oc}, thus the efficiency. The so called PERC structure (Passivated emitter and rear cell) is described by Green in [2], depicted in **Figure 1.4 i)**, with the following advantages: reduction of rear surface recombination by a combination of an insulator surface passivation and reduced metal/semiconductor contact area, with simultaneously increased rear surface refection. Nevertheless, to bring this feature to CIGS solar cells, both the minority and majority carrier diffusion lengths have to be well known, that are orders of magnitude lower than in the Si solar cells. In CIGS solar cells, to do point contacts, they must have an appropriate spacing and avoid minority carrier losses, as it is shown in **Figure 1.4 ii)**.

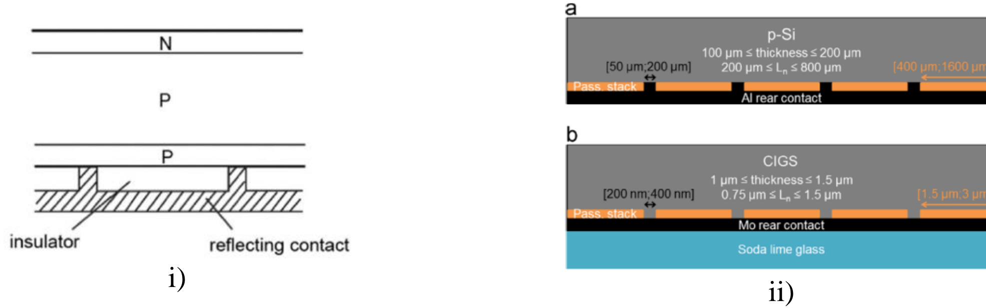

Figure 1.4 – i) First diagram of PERC structure [2]. ii) Schematic representation of the rear of (a) a p-type Si solar cell with a surface passivation stack and micron-sized local point contacts and (b) a CIGS solar cell with a surface passivation stack and nano-sized local point contacts. Also, typical base/absorber thickness, minority carrier diffusion length (L_n), contact opening diameter and distance between contact openings are specified [18].

Nowadays, it is common practice to use Al_2O_3 as an insulator deposited by ALD in silicon solar cells technology [32,33]. Other materials are being the focus of many research teams like TiO_2 [34] and ZnS [35,36]. Possible candidates, such as, HfO_2, SiO_2 and Si_3N_4 are also referred in literature [24]. The thickness of the passivation layer and the deposition conditions are also a matter of study to reach the best passivation possible, integration of other advanced light trapping techniques and studying other candidates for the passivation layer [13]. The study of other types of passivation layers, as well as, the most suitable deposition conditions are the purpose of this thesis.

1.4. MIS structures

Metal-Insulator-Semiconductor (MIS) structures are of special importance in the field of electronics and can be used in optoelectronics to extract relevant device parameters. Particularly, performing MIS measurements, it is possible to study the electronic properties of the insulator-semiconductor interface. More precisely, with MIS measurements, it is possible to identify the interface density of defects/traps. Regarding the study of different types of passivation, the density of interface defects (D_{it}) related to the already mentioned chemical passivation, is accomplished by performing C-G-f measurements, whereas the number of fixed insulator charges estimation (Q_f) related to the field-effect passivation, is reached through C-V-f measurements. In order to do the different measurements, it is necessary to understand the different MIS conditions in the C-V curve, namely the accumulation, the depletion and inversion regions, as it is shown in **Figure 6.6** of **Annexes**.

1.4.1 Fixed insulator charges (Q_f)

To extract Q_f it is necessary to perform C-V measurements, at selected frequencies, to understand the depletion/weak-inversion transition region.

The Q_f is calculated by [22,37]:

$$Q_f = \frac{C_{in}(\phi_{MS} - V_{fb})}{A \times q} \tag{4}$$

where ϕ_{MS} is the work function difference between the metal and the semiconductor, A is the metal surface area, q is the elementary charge, V_{fb} is the flat-band voltage, that will be explained in more detail later and C_{in} is the insulator capacitance value extracted in strong accumulation condition of a C-V curve.

The flat-band voltage is of special interest in this calculation, being the voltage required to make the energy bands to be flat, when a charge is present inside the insulator, as shown in **Figure 6.7** of **Annexes**.

Several methods are presented by Piskorski *et al.* [38] to calculate the V_{fb}. In this work we used the graphical method, also known as the $[(C_{in}/C_m)^2-1](V_G)$ method, shown in **Figure 1.5**.

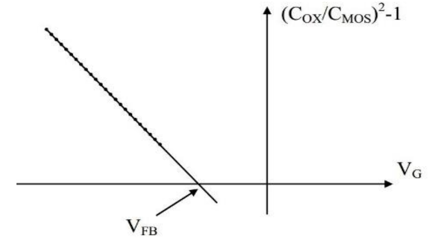

Figure 1.5 - V_{fb} is extrapolated from the linear part of $[(C_{in}/C_m)^2-1](V_G)$ characteristic to the zero value [38].

1.4.2 Density of interface defects (D_{it})

To extract D_{it}, several methods are reported in the literature for silicon and GaAs devices [37]. The Conductance Method introduced by Nicollian and Brews [22,39], is used in this thesis. It is the most accurate density of interface defects extraction method and insensitive to parasitic effects [39,40].

The Conductance Method is based on the equivalent circuit, presented in **Figure 1.6 a)**, where C_{in} is the insulator capacitance, C_s is the semiconductor depletion layer capacitance, C_{it} and R_{it} are the capacitance and resistance associated with the interface-traps. The parallel circuit in **Figure 1.6 a)** can be converted into a frequency-dependent capacitance C_p and a frequency-dependent conductance G_p, as shown in **Figure 1.6 b)**. In **Figure 1.6 c)**, C_m is the measured capacitance and G_m is the measured conductance which is the circuit that the measuring equipment uses. The relations between C_p and G_p are given by [40]:

$$C_p = C_s + \frac{C_{it}}{1 + \omega^2 \tau_{it}^2} \quad (5) \qquad \text{and} \qquad G_p = \frac{C_{it}\omega^2\tau_{it}}{1 + \omega^2 \tau_{it}^2} \quad (6)$$

where τ_{it} is the interface-trap lifetime and ω is the angular frequency.

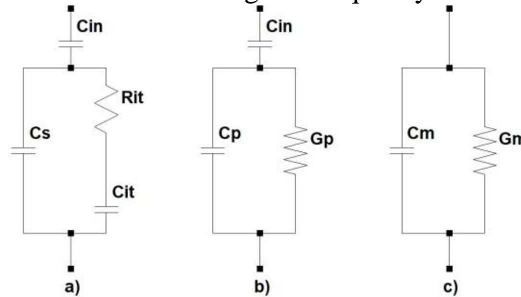

Figure 1.6 - Equivalent MIS circuits for conductance measurements: a) including interface-trap effect; b) simplified circuit of a); c) device's measured circuit.

Plotting (G_p/ω) against the frequencies (f) will yield a maximum in the energy loss mechanism. The maximum gives direct information about the density of interface defects [37]. The relation is given by [22,41]:

$$D_{it} = \left(\frac{2.5}{A \times q}\right)\left(\frac{G_p}{\omega}\right)_{max} \quad (7)$$

where $\left(\frac{G_p}{\omega}\right)$ is calculated accordingly by [22,39]:

$$\left(\frac{G_p}{\omega}\right) = \frac{\omega G_m C_{in}^2}{G_m^2 + \omega^2 (C_{in} - C_m)^2} \quad (8)$$

where C_{in} being the measured capacitance in strong accumulation.

2 Materials and methods

The main focus of this work is the study of the effects of several insulators types, namely aluminium oxide (Al_2O_x), silicon nitride (Si_3N_x) and silicon oxide (SiO_x), on the CIGS interface properties. Taking into account that only two 5x5 cm^2 SLG/Mo/CIGS/CdS samples were available, a carefully experimental planning was needed to account for the differences between the insulators types and deposition methods. It is necessary to understand that the two samples of material were made in the same day and the same way, however, due to the inhomogeneous CIGS deposition, differences between them might not make possible comparisons between the two CIGS pieces. Hence, the experimental planning had also to account for sample inhomogeneity by having a reference in each of the two samples.

The samples were made of soda-lime glass substrate (2 mm), molybdenum back contact (350 nm), $Cu(In_{1-x},Ga_x)Se_2$ as absorber layer (2 µm) and cadmium selenide (CdS) (70 nm) on top of it to prevent air exposure to the CIGS during handling [42,43]. The Mo deposition was carried out by DC-sputtering and the CdS deposition was done by chemical bath deposition. The CIGS deposition occurred in Uppsala University by co-evaporation, accordingly to Ångström solar cell baseline, with a thickness of approximately 2 µm. There is a Ga gradient from [Ga]/([Ga]+[In]) = 0.25 at the front contact to 0.65 toward the rear contact, which corresponds in a rear contact bandgap energy of 1.14 eV to 1.38 eV in the front contact [44].

The following section presents the experimental planning to understand the succeeding results and discussion in the next chapter.

2.1. Experimental planning

Two samples with 5x5 cm^2 were cut, using a pen with a diamond point, into four smaller samples of 2.5x2.5 cm^2 as it is shown in **Figure 2.1**.

In order to a better understanding of each sample name, **Table 1** shows the names used hereafter.

Table 1 – Sample's names used hereafter, considering the deposition used and the respective CIGS piece.

CIGS A		**CIGS B**	
CIGS A reference sample	A - CdS	CIGS B reference sample	B - CdS
Al_2O_3 deposited by sputtering	A - Al_2O_3 - S	SiO_x deposited by PECVD at 300 ºC, HF	B – SiO_x – 300 ºC
Si_3N_x deposited by PECVD at 150 ºC, HF	A – Si_3N_x	SiO_x deposited by PECVD at 150 ºC, HF	B – SiO_x – 150 ºC, HF
Al_2O_3 deposited by ALD	A - Al_2O_3 - ALD	SiO_x deposited by PECVD at 150 ºC, LF	B – SiO_x – 150 ºC, LF

On the first CIGS piece (CIGS A), the main focus was the Al_2O_3, which is a well-known passivation layer for silicon solar cells. Two different deposition techniques were used in order to understand which one is more suitable: sputtering and atomic layer deposition (ALD). Also, in this CIGS piece, a sample of Si_3N_x was deposited to comprehend the differences between Si_3N_x and Al_2O_3. In the second CIGS piece (CIGS B), the same technique (PECVD) and the same material (SiO_x) were used to reach the ideal deposition conditions. It is noted that in both CIGS pieces, one sample of SLG/Mo/CIGS/CdS remained intact, to serve as the reference for each CIGS piece. The planning representation is shown in **Figure 2.1**.

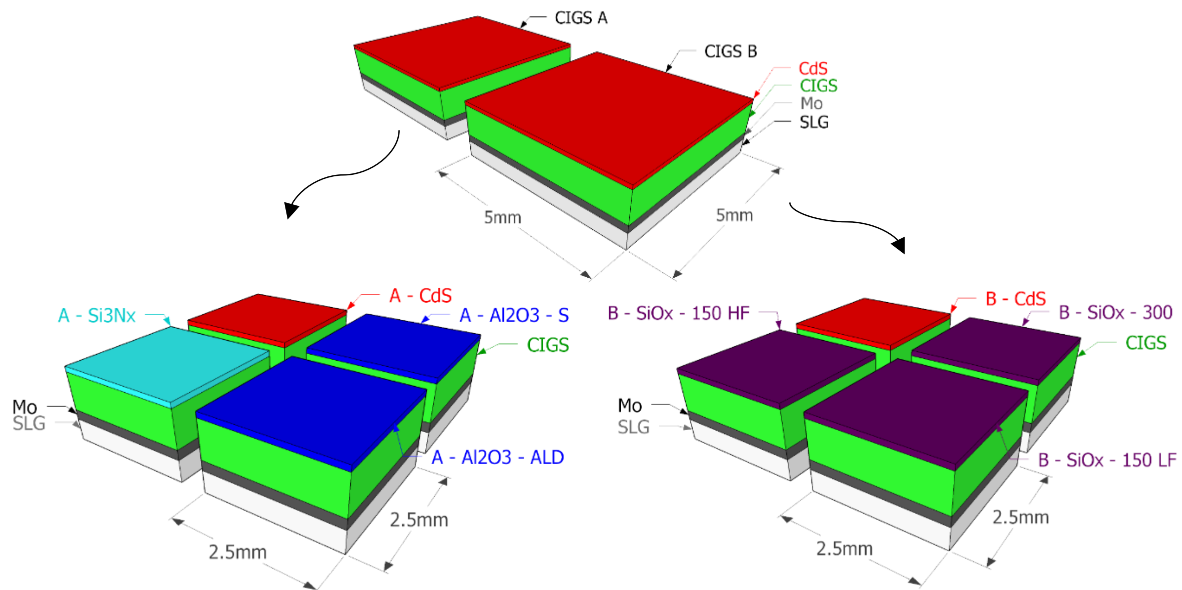

Figure 2.1 – Experimental planning for the used CIGS pieces. Each CIGS piece was divided into four samples. The CIGS A is to compare different types of depositions mostly with Al_2O_3 (dark blue) and Si_3N_x (light blue). The CIGS B aims to compare the same deposition technique (PECVD) with the same material SiO_x (purple) at different depostion conditions, namely different temperatures and deposition frequencies. A - CdS and B - CdS (red) represent the reference samples for each CIGS piece. The layers are not at scale.

2.2. MIS fabrication and depositions techniques

This section aims to explain the insulator deposition, since it was the only fabrication step done in this work. It is necessary to understand that the CIGS's air exposure is a degrading process which severally affects the CIGS surface. Thus, by doing a CdS coverage, the CIGS surface will remain pristine, even after the CdS removal. However, the CdS removal should be a fast process in order to avoid the CIGS air exposure.

Before the insulator deposition, the CdS removal was necessary, as it is shown in **Figure 2.2**. In order to do the CdS removal, 10 % (w/w) HCl was used during 2 min to etch the CdS layer [45]. Subsequently, the sample was taken to the deposition tools in a matter of seconds to avoid CIGS air exposure.

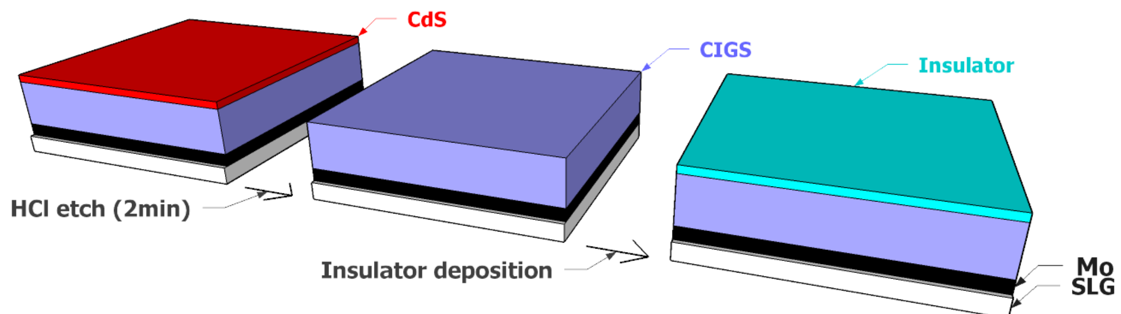

Figure 2.2 - HCl etch of CdS and subsequent insulator deposition. The layers are not at scale.

Several insulator materials with a thickness of 50 nm were deposited using different techniques:

i) Aluminium oxide (Al_2O_3) by sputtering, using a Metallization Singulus Sputtering tool (Timaris FTM). The deposition was carried out by a standard INL recipe to deposit specifically 50 nm. The RF mode was used at 1500 W and argon injection with a flow of 200 sccm. The starting pressure was $7x10^{-8}$ mbar increasing with the argon injection, being the deposition pressure unknown. The substrate temperature is not intentionally

increased, however, due to the proximity to the Al_2O_3 target, it can reach temperature values as high as 200 ºC.

ii) Silicon nitride (Si_3N_x) by Plasma Enhanced Chemical Vapour Deposition (PECVD), using SPTS MPX CVD tool at 150 ºC, High Frequency (HF) of 13.56MHz, plasma power of 30 W and as precursor gases NH_3, $SiH_{4\text{-}5}$ and N_2.

iii) Silicon oxide (SiO_x) by PECVD, using the same tool at three different deposition conditions: 300 ºC and 150 ºC, HF, plasma power of 30 W and as precursor gases N_2O, $SiH_{4\text{-}5}$ and N_2; 150 ºC, low frequency (LF) of 380kHz, plasma power of 60 W and the same precursor gases.

iv) Aluminium oxide (Al_2O_3) by atomic layer deposition (ALD) was done in Uppsala University at 200 ºC, using as precursor gases Trimethyl aluminum (TMA) as aluminum source and H_2O as oxygen source.

Another set of insulator depositions, with the same conditions as the ones describe before, were carried out in silicon substrates in order to evaluate the film thickness. The thickness measurement was done using a contact profilometer (KLA TENCOR P-16+). We reached the conclusion that all deposition techniques accomplish thicknesses in the order of 50 nm corresponding to the required value.

To create the MIS structure, the metal aluminium layer front contact, was deposited at the Faculty of Science and Technology, New University of Lisbon. These contacts were done by thermal evaporation, with an initial pressure of $5x10^{-6}$ mbar, in two steps: 200 nm deposition thickness in each step, to accomplish the desired 400 nm with the pattern shown in **Figure 2.3**:

Figure 2.3 Mask used in the aluminium thermal evaporation. Holes with three diameters: 1 mm, 2 mm and 3 mm.

The final scheme of one MIS structure and a representative SEM cross-section are depicted in **Figure 2.4**.

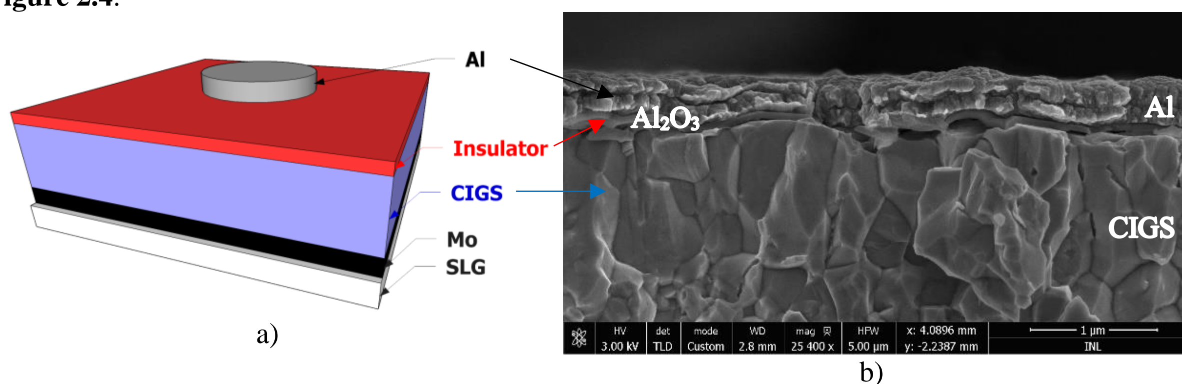

Figure 2.4 a) Scheme of MIS structure: SLG/Mo/CIGS/insulator/Al. The molybdenum thickness is 350 nm, the CIGS is 2 µm, the insulator 50 nm and the aluminium layer 400 nm (bilayer of 200 nm each). The image is not at scale. b) SEM cross-section of sample A – Al_2O_3 – S.

2.3. Characterization techniques

The CIGS surface characterization must be done to better understand the possible damage of each deposition and the electrical interface performance between the insulator and the CIGS after the deposition. Raman spectroscopy, x-ray diffraction, photoluminescence and time-resolved photoluminescence analysis were performed to characterize the CIGS interface, thus the damage impinged by the insulator deposition. Electrical measurements were done to better understand the insulator/CIGS interface, namely if a low density of interface defects is accomplished.

Raman spectroscopy was done, using Confocal Raman Microscope 300 R (WiTec) with green laser (excitation wavelength of 532 nm), 1 mW of power and a Zeiss objective of 100x in the backscattering configuration.

X-ray diffraction (XRD) was conducted using PANalytical's diffractometer system XPERT-PRO with a cooper source K_α (wavelength 1.540598 Å), using Bragg-Brentano theta-2theta configuration.

Photoluminescence (PL) and Time-resolved photoluminescence (TRPL) were performed at IMEC in Belgium. It was used a YAG, class 3B laser with a 15kHz repetition rate and 1 ns pulse length with a beam spot of 3 mm and excitation wavelength of 532 nm. An average illumination intensity of 1 mW was used. TRPL was checked at the excitation wavelength that matched the PL peak in each case varying from 1090 to 1125 nm. In order to extract lifetime values, a common procedure is to use a second order fitting (bi-exponential decay model) which was the selected method used in this work.

Scanning electron microscopy (SEM) cross-section was carried out, using the NovaNanoSEM 650 tool with an acceleration voltage of 3kV.

The techniques used so far, were to study changes in the CIGS properties, more precisely in the interface with the insulator. From now on, Metal-Insulator-Semiconductor (MIS) measurements were done to study the electrical properties of the CIGS/insulator interface.

C-G-f measurements were done in Agilent E4890 A with 30 mV (V_{RMS}), 0V in V_{bias}, 1m cable correction and 10 iterations with a medium iteration time, from 20 Hz to 1 MHz. C-V-f measurements were done in the same tool with 30 mV (V_{RMS}), a frequency of 10 kHz, 1 m cable correction and 10 iterations with medium iteration time with different V_{bias} ranges, depending on the samples and front contact area.

Simulations of the MIS structure model were performed in the ZSimpWin 3.50 software. This software allowed for detection of shunted cells, as well as the appropriate fitting model for each working cell.

2.4. Electrical measurement tool

At the beginning of the master thesis, there was no electrical measurement tool and nobody in the group knew the electrical measurements know-how. Keeping in mind that the MIS measurements were needed, we start looking into de INL's groups and we found that two tools were available to do the electrical measurements, namely the AUTOLAB system PGSTAT302N, henceforth called AUTOLAB, and the LCR Agilent E4890 A, hereafter called LCR. Despite the AUTOLAB been mostly used by chemistry users, it allows us to perform the measurements that we need. In order to study the both tools limitations, a considerable amount of experimental planning was done using solar cells. Initially, MIS structures were not used due to the fact that we did not know what to expect from the measurements. However, from the solar cells we knew very well the behaviour under certain conditions, therefore they were the perfect testbed.

The AUTOLAB was not designed to measure solar cells, however, this tool has the electrical measurements procedures already defined with the possibility to change the measurement parameters, namely the V_{bias}, the V_{RMS}, the integration time, the frequency, among others. We began with a "dummy cell" to serve as a test cell, in order to calibrate the device. After the test cell measurements, therefore the system calibration, we began to understand better the operation of the equipment. Subsequently, several measurements were carried out on passivated CIGS solar cells and on standard CIGS solar cells. Initially, we began with I-V curves under dark conditions and the obtained curves were not what we

expected. We started the measurements with crocodile clips, however due to the unexpected results, a change to BNC cables connected to micro positioners with tips were done and the I-V curves started looking as they should be. It is noted that in order to understand the functionality of the different cables, an experimental planning was done under the same conditions, only varying the parameter that we wanted, in this case, the change from crocodile clips to micro positioners with tips. More experimental planning was done, namely the experience of measuring the cells with and without light soaking done before the measurements, changing the integration times and number of cycles, changing the V_{RMS} values, among others. Then, Mott-Schottky, as well as, C-f and N-w measurements were done as it is shown in **Figure 2.5.**

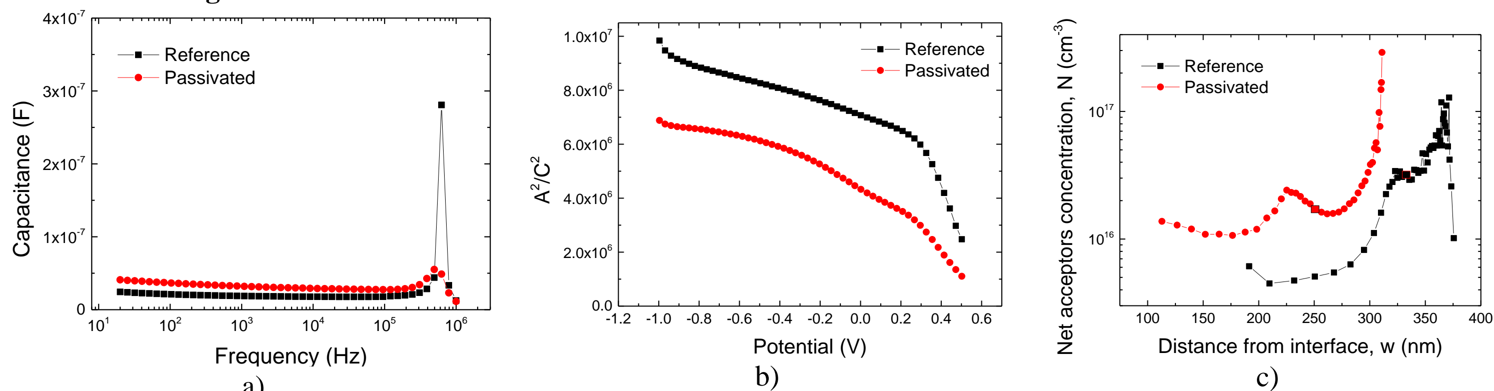

Figure 2.5 - Measurements of reference and passivated cell: a) C-f curve; b) Mott-Schottky curve and c) N-w curve

The outcomes started to be as expected, and a very well-defined procedure for Mott-Schottky measurements was established. The results were used as complementary measurements in a poster[1] presentation and for a paper[2] publication.

After several measurements, and as it is shown in **Figure 2.5 a)**, the AUTOLAB had limitations at high values of frequency. Also, after C-V measurements performed to MIS structures, one realized that the equipment was not able to go below -2V and above 2V, thus C-V measurements were highly limited. The use of LCR device started, and comparisons between the two equipment were done.

By default, in the measurements, the LCR assumes the C_p-R_p parallel circuit. However, the AUTOLAB assumes the same equivalent circuit with a series resistance. This series resistance value should be inserted by the user and, consequently, it should be well known for each device under test. An experimental planning was done to compare several parameters, such as the series resistance change, the V_{RMS} change, and their influence on the results, as it is shown in **Table 2**.

[1] P.M.P. Salomé, J.P. Teixeira, M.A.M. Cardoso, V. Fjällström, P.A. Fernandes, J.M.V. Cunha, M. Edoff, N. Nicoara, J.P. Leitão, S. Sadewasser, "Analysis of waiting times between CIGS and CdS and in-diffusion of Na on the properties of $Cu(In,Ga)Se_2$ materials and solar cells", presented in 2017, April 17-21, MRS in Phoenix, Arizona.

[2] P.M.P. Salomé, Bart Vermang, R. Ribeiro-Andrade, J.P. Teixeira, J.M.V. Cunha, M. J. Mendes, S. Haque, J. Borme, H. Aguas, E. Fortunato, R. Martins, J.C. González, J. P. Leitão, P.A. Fernandes, M. Edoff and S. Sadewasser, "Passivation of interfaces in thin film solar cells: understanding the effects of a nanostructured rear point contact layer", submitted to *Advanced Materials Interfaces*.

Table 2 - Representative experimental planning of the AUTOLAB system and LCR comparisons.

AUTOLAB		
Solar Cell (Reference)	Si_3N_x (MIS with 3 mm)	SiO_x (MIS with 3 mm)
4Ω + V_{RMS}=10mV	R_s = 4Ω + V_{RMS}=10mV	R_s = 4Ω + V_{RMS} = 10mV
4Ω + V_{RMS}=35mV	R_s = 4Ω + V_{RMS}=35mV	R_s = 4Ω + V_{RMS} = 35mV
New Rs + V_{RMS}=10mV	New Rs + V_{RMS}=10mV	New Rs + V_{RMS} = 10mV
New Rs + V_{RMS}=35mV	New Rs + V_{RMS}=35mV	New Rs + V_{RMS} =35mV
LCR		
Solar Cell (Reference)	Si_3N_x (MIS with 3 mm)	SiO_x (MIS with 3 mm)
Cp-G , V_{RMS} = 10mV	Cp-G , V_{RMS} = 10mV	Cp-G , V_{RMS} = 10mV
Cp-Rp , V_{RMS} = 10mV	Cp-Rp , V_{RMS} = 10mV	Cp-Rp , V_{RMS} = 10mV
Cp-G , V_{RMS} = 35mV	Cp-G , V_{RMS} = 35mV	Cp-G , V_{RMS} = 35mV
Cp-Rp , V_{RMS} = 35mV	Cp-Rp , V_{RMS} = 35mV	Cp-Rp , V_{RMS} = 35mV

After several tests in both AUTOLAB and LCR, we choose the LCR due to be the more accurate tool, with less parameters to change and, apparently, with less limitations. However, it had limitations too, at very low and vert high frequencies due to the cables configuration.

The measurements of the Gp/ω against the frequencies were initially quite complex as there was no experience in the group and the literature on the measurements conditions is very scarce. Experimental planning with silver ink on the front metal of the MIS structures and scribing of the MIS structures were made in order to understand their influence on the measurements. Several tests were done until the final method to perform the electrical measurements was accomplished.

3 Results and Discussion

In this chapter, each result will be shown and discussed. Firstly, we need to take into consideration if the deposition of the insulator caused any damage to the CIGS, thus, in this case we will be taking conclusions about the deposition technique and the deposition conditions used. Then, it is needed to understand, even if the CIGS surface and bulk are not damaged, if electrically the structure is working well, in other words, if the insulator material is actually passivating the CIGS layer, keeping a good electrical performance.

First, to analyse the CIGS layer, namely possible CIGS surface damage or modification, due to the insulator deposition, Raman scattering was performed since it is a shallow measurement which allows us to identify surface changes. In order to understand if bulk CIGS damaging occurred as well, X-ray diffraction was done due to be a bulker measurement technique. As complementary techniques, photoluminescence was taken to study the CIGS defects and time-resolved photoluminescence was done to study the carrier's lifetime.

Finally, with the MIS structures completed, to study the structure electrical performance, measurements were performed to reach the fixed insulator charges and the density of interface defects.

All techniques together, will allow us to reach the effects of the passivation layer to be used together with the best deposition technique.

3.1. Raman spectroscopy

In this section, we aim to understand if the CIGS surface was modified or damaged, due to the CdS removal and/or due to the insulator deposition. Since the Raman technique is a shallow measurement, mostly surface variations are observed. Raman spectra for each sample are depicted in **Figure 3.1**.

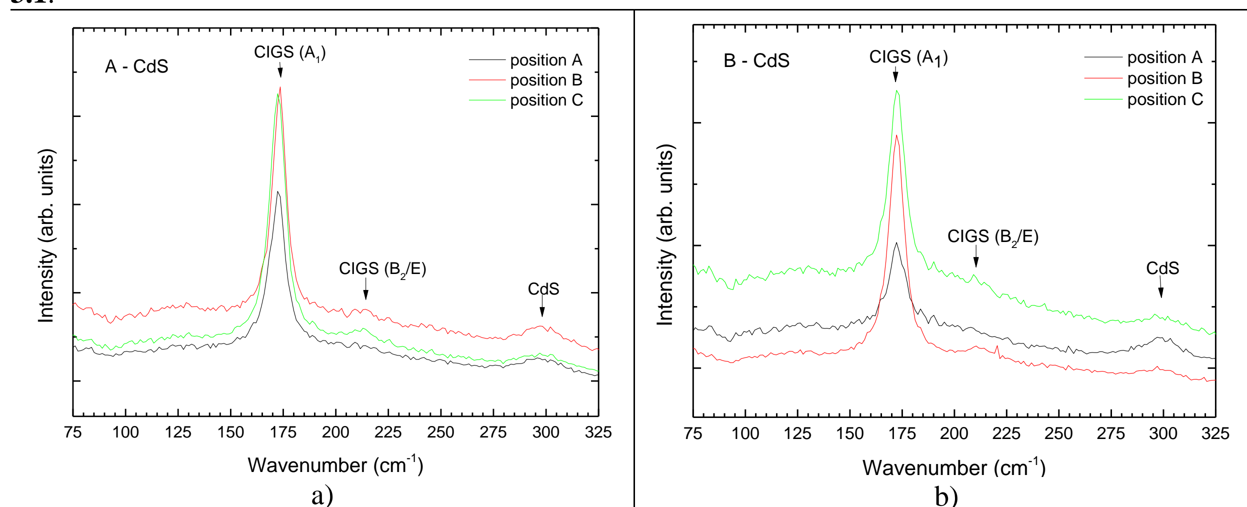

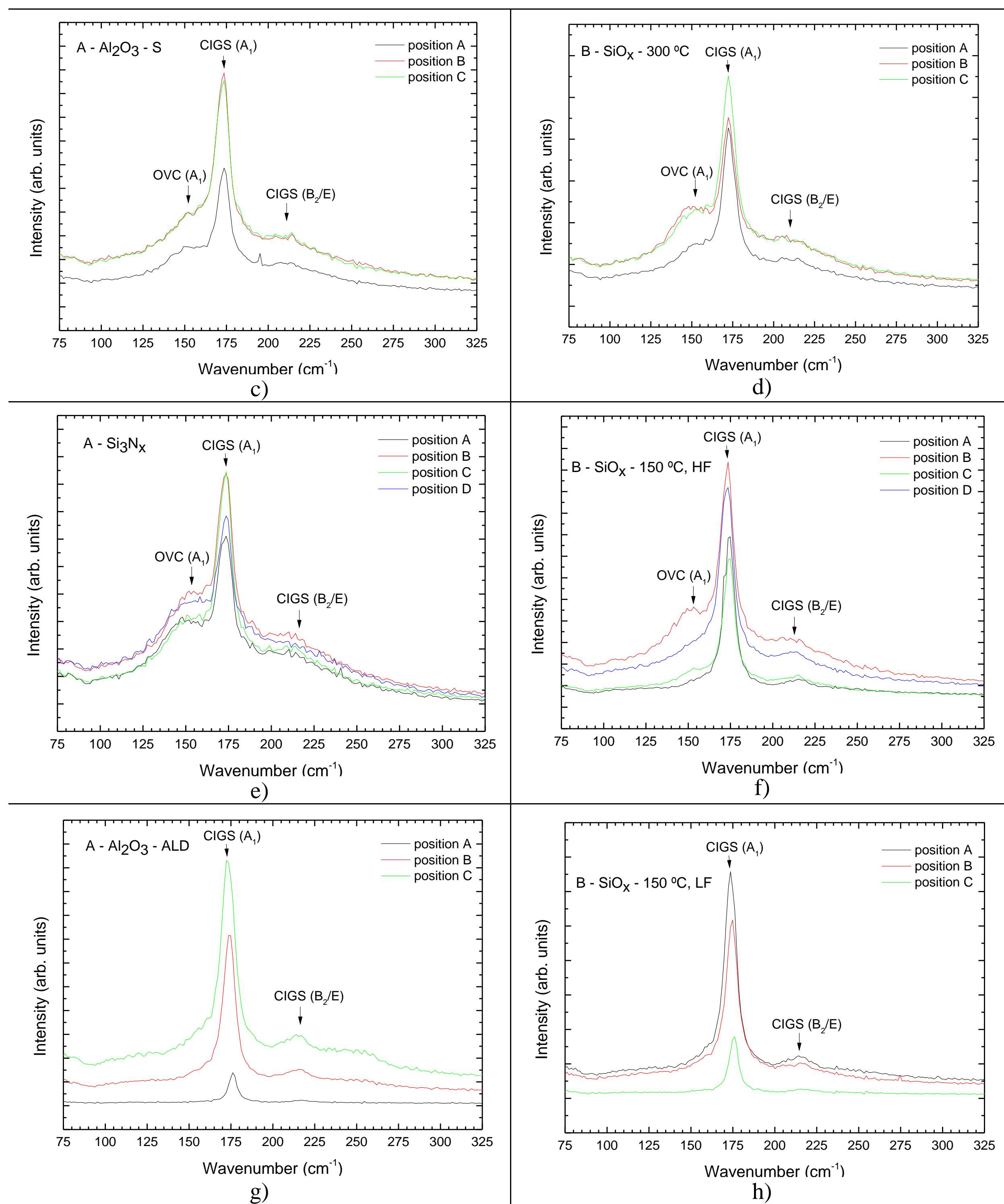

Figure 3.1 Raman spectra of CIGS A in the left side and CIGS B in the right side. Each curve represents different spots in the same sample: a) A - CdS; b) B - CdS; c) A - Al_2O_3 - S; d) B - SiO_x - 300 ºC; e) A - Si_3N_x; f) B - SiO_x - 150 ºC, HF; g) A - Al_2O_3 - ALD and h) B - SiO_x - 150 ºC, LF.

First, we measured the reference sample of the CIGS A, since the CIGS layer was pristine and only the CdS was deposited to serve as a protective layer, taking into consideration that the CdS deposition does not damage the CIGS layer. As it is shown in **Figure 3.1 a)**, in the A – CdS sample, it is clearly visible the main CIGS peaks, namely the narrow CIGS A_1 mode peak centred at 172 cm^{-1} [46], and the broader CIGS B_2/E modes peaks appearing between 210 cm^{-1} and 227 cm^{-1} [47]. Also, since

Raman probes mostly the top-most part of the sample, the layer of CdS is noticeably visible at 300 cm^{-1} peak [48]. The different curves represent different locations in the sample. In **Figure 3.1 b)**, it is visible that the B - CdS sample is similar with the same peaks represented, showing good uniformity between the CIGS pieces. Also, in the Annex section, **Figure 6.1 a)**, the B – CdS sample was measured in the same spot, with different focus points. The objective of doing so was to understand if there is uniformity in depth. In this case, the peaks are unchanged. Such fact means that the reference samples are uniform in depth as well as in the 2D plane.

In **Figure 3.1 c)** it is seen the Raman spectrum of the A - Al_2O_3 - S sample, being the main CIGS peaks remained the same, with the difference that a "shoulder" is appearing near to the A_1 mode peak, at approximately 153 cm^{-1}. This peak is attributed to an ordered vacancy compound (OVC) [46,49]. The presence of the OVC can possible be attributed to the fact that the CIGS surface was modified [49], most likely due to loss of cooper during the high energy sputtering process or by the HCl etching of the CdS. It is known that the CIGS surface is quite sensitive to sputter damage [50] and that the HCl etching should not cause damage to the CIGS surface [45]. Thus, we link the appearance of the OVC phase at the surface of the CIGS to surface damage induced by the sputtering of the Al_2O_3 layer. The possibility of the HCl etching causing surface damage was discarded after an experiment. This experiment was prepared with a small piece of one of the reference samples. Raman scattering was conducted just before the CdS etch and right after it. Both spectra are shown in the Annex section, **Figure 6.2 a)** and **Figure 6.2 b)** and there are no observable differences before and after the spectra reinforcing the fact that the etch does not causes damages to the CIGS surface. Furthermore, the OVC phase is not seen in all of the samples, as it is shown in **Figure 3.1**. Both reference samples, the A - Al_2O_3 - ALD sample and the B - SiO_x - 150 ºC, LF sample do not have the Order Vacancy Compound. The B - SiO_x - 150 ºC, HF sample appears to not have the OVC phase, however, one of the measurements have the "shoulder", thus, the OVC phase can be present. Nevertheless, the A - Al_2O_3 - S, the A - Si_3N_x and the B - SiO_x - 300 ºC samples clearly have the OVC phase. As it was mentioned before, the OVC phase of the A - Al_2O_3 - S sample could be due to the deposition method used (sputtering), the OVC phase of the B - SiO_x – 300 ºC sample could be explained taking into account the CIGS surface damage imposed by the high temperatures involved in the insulator deposition. The A - Si_3N_x deposition was the same as the B - SiO_x - 150 ºC, HF sample, being the only difference, the precursor gases used, namely the ammonia (NH_3), which can be damaging the CIGS surface and consequently appearing the OVC phase.

Since the "shoulder" is appearing in only one measurement of the B - SiO_x - 150 ºC, HF sample, as it is shown in **Figure 3.1 f)**, it means that the sample is not uniform due to each measurement was conducted in different spots of the same sample. It is necessary to understand that the Raman scattering is limited by localization, in other words, since the laser diameter is considerably smaller than the sample's area, the measurement is highly localized, thus, it is difficult to have a good statistic of the entire sample. Consequently, this can be the explanation to the appearance of the OVC "shoulder" in some measurements of the same sample and not in the others, as it was concluded for this B - SiO_x - 150 ºC, HF sample. This is the reason why several measurements were performed and shown.

Another test was conducted, precisely the Raman measurement in the same spot with different focus points to comprehend the uniformity in depth, in other words, if the OVC phase is present in depth. It is shown in **Figure 6.1** of the **Annexes**, all the measured samples in the same spot with different focus points. The conclusions are the same for the measured samples in different spots, although, the B - SiO_x - 150 ºC, LF now appears to have the OVC phase, and it was not seen in the previous measurements, thus, this sample is not uniform in depth.

In summary, and knowing that atomic layer deposition is one of the most used deposition techniques for the passivation layer [18,29,41,51,52], the A - Al_2O_3 - ALD (not considering the reference samples), is the only one showing uniformity both in the surface 2D and in depth.

In order to understand if the CIGS layer modification is only a shallow one or a bulker one, X-ray diffraction was conducted, due to be a bulker measurement than Raman. It is possible to see the discussion in the next section.

3.2. X-ray diffraction

The X-ray diffraction technique in the Brag-Brentano (teta-2teta), is mostly a bulk measurement. Hence, by comparing the XRD results with the Raman, one is able to say if the changes to the samples are localized at the surface or being propagated into the bulk of the film.

All samples had virtually the same XRD graphs, thus, only one is presented in **Figure 3.2** and all the others are in **Annexes**, **Figure 6.3**.

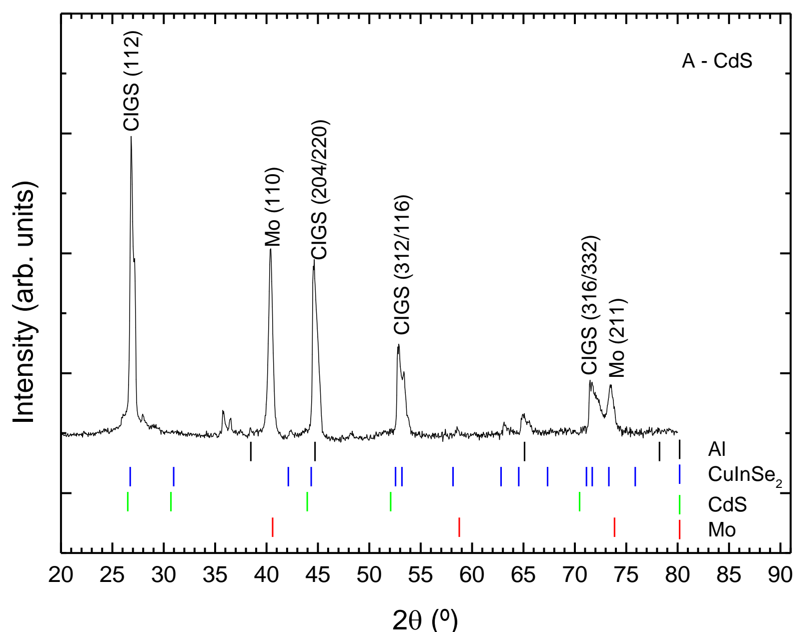

Figure 3.2 Reference sample's X-ray spectrum of CIGS A with Mo, Al, CdS and $CuInSe_2$ crystalline planes identified.

As it is shown in **Figure 3.2**, the main CIGS XRD peak is present at 26.8 º corresponding to the crystalline plane (112). Other CIGS crystalline planes are present, namely (204/220) at 44.7 º, (312/116) at 52.8 º and (316/332) at 71.4 º [53]. Molybdenum related peaks are also present at 40.4 º corresponding to the crystalline plane (110) and 73.4 º matching to the crystalline plane (221). It is noted that the cadmium sulphide and aluminium related peaks do not appear in the XRD spectra. The fact that the CdS and Al peaks are not appearing is expected taking into account that the mentioned layers are thin layers on top of the CIGS layer. Thus, it is expected that none of the deposited insulators are also seen, as it is shown in **Figure 6.3**. Moreover, in **Figure 6.3 i)**, the samples are presented all together, including the references, with no visible differences between them.

In order to be sure that the samples are without bulk defects, a zoom will be done to the CIGS main peak at 26.8 º, corresponding to the (112) crystalline plane. As it was mentioned in before**,** we only should compare the insulators from each CIGS piece individually, thus the samples corresponding to CIGS A are shown in the Annex section, **Figure 6.4 a)** and the samples corresponding to CIGS B are shown in **Figure 6.4 b)**. Both CIGS pieces have the same main peak at 26.8 º, with no changes between the reference samples and the insulator deposited samples. It is clearly visible two peaks, which is a characteristic feature of the Ga grading CIGS solar cells [11].

In conclusion, no differences between the reference samples and the insulator deposited samples in each CIGS piece were found, thus the CIGS layer changes due to the insulator deposition only happened at the CIGS surface, as it was shown in Raman measurements, but not at the bulk of the CIGS layer, since the X-ray diffraction did not show changes in the peak before and after the insulator deposition.

3.3. Photoluminescence

In this work, Photoluminescence (PL) was used to qualitatively study the defect concentrations by looking at the emission width and number of peaks present. In general, the higher the number of peaks and the wider they are, the more defects are affecting the PL emission. Such approach is a very simple one, considering the potential of PL analysis, however, it is commonly done like this in passivation studies due to the complexity of the PL interpretation [54,55].

For the sake of comparison, only the depositions made in CIGS A were compare together in **Figure 3.3 a)** and the ones made in CIGS B are shown in **Figure 3.3 b)**.

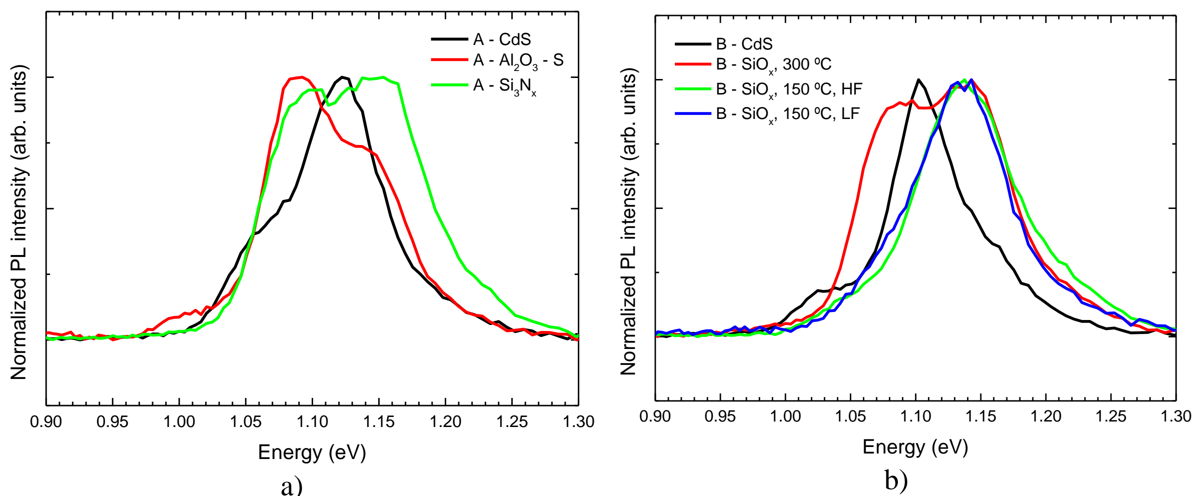

Figure 3.3 – Photoluminescence spectra of: a) CIGS piece A samples. b) CIGS piece B samples.

In the CIGS piece A, shown in **Figure 3.3 a)**, the A - Al_2O_3 – S and the A - Si_3N_x samples show more than one peak, possibly meaning that, in both, more than one type of defect is present. Also, taking into account the A - Si_3N_x sample, the peak is broader than the A - Al_2O_3 - S. Another feature visible in the graph, is that the A - Si_3N_x peaks do not have the same reference sample position. Nonetheless, the A - Al_2O_3 - S sample have one of the peaks positioned in the same place of the reference sample peak, with less intensity, and the other at lower energies.

Taking into consideration the CIGS B, shown in **Figure 3.3 b)**, only the silicon oxide deposited at 300 ºC has two peaks, even so the silicon oxide deposited at 150 ºC HF and LF have only one peak. All the three samples with insulator on it have one peak in the same position, although different from the reference sample, being at higher energies, more precisely, a blueshift happened. A blueshift of the emission can be correlated with either a higher value of bandgap, which seems unlikely to these samples due to the Raman results, or to passivation of shallow defects [54].

The Al_2O_3 deposited by ALD sample was not available when sent to Belgium where the Photoluminescence was carry out as well as time-resolved photoluminescence.

In conclusion, the SiO_x deposited by PECVD at 150 ºC, HF and the SiO_x deposited by PECVD at 150 ºC, LF have only one narrow peak, being both samples with less defects than the others.

In the next section time-resolved photoluminescence will be shown, to understand if a correlation between all the techniques done so far is approachable.

3.4. Time-resolved photoluminescence

The time-resolved photoluminescence (TRPL) technique was used to extract the samples minority carriers' lifetimes.

In **Figure 3.4**, the carriers' lifetimes are shown. Since the reference samples have much higher carriers' lifetimes than the insulator deposited samples, a graph only with the deposited samples is shown separately. This may be happening because of an electrical field created by the p-n junction

between the CIGS and CdS which increases the carries' lifetime and on the other hand, when the insulator is present, there is no p-n junction, thus, the comparison of lifetime values is not valid. It is noted, again, that the A - Al_2O_3 - ALD is not presented due to the same reason mentioned in the Photoluminescence section.

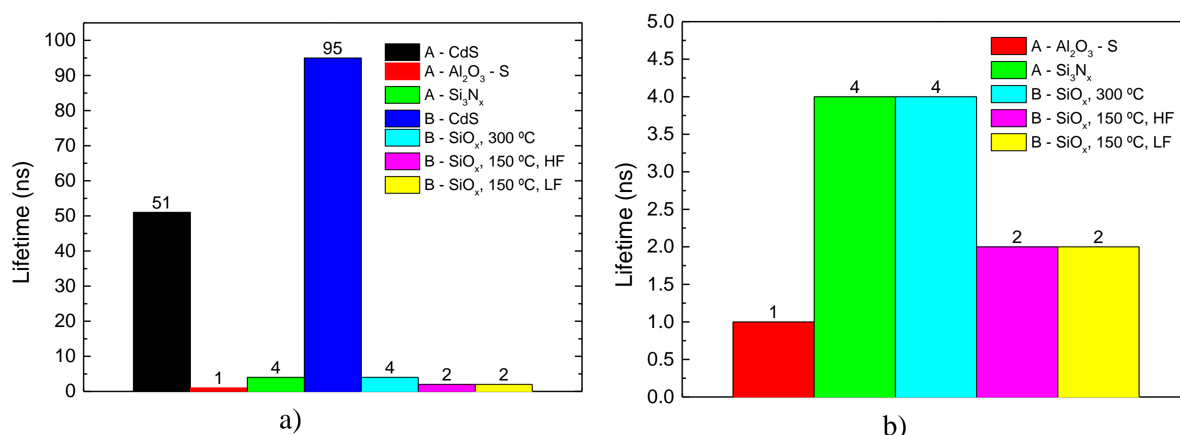

Figure 3.4 – Minority carriers' lifetime of: a) All samples together including the reference samples; b) Only samples with insulator deposition without the reference samples.

It is clearly visible in **Figure 3.4**, in the left graph, a huge difference between the reference samples and the deposited ones, considering the p-n junction, as it was mentioned before. On the other hand, the results only between the deposited samples are inconclusive, because they are all inside error values. One possible explanation is that the model used here (bi-exponential decay model) is not the best fitting model for these MIS structures. Depending on the dominant type of recombination, other types of models can apply, and thus, at this moment of interpretation of TRPL data is very controversial in the literature [56,57]. Due to the complexity of identifying the exact model, this task is outside the scope of this thesis.

3.5. Raman and photoluminescence results overview

In **Table 3**, it is presented a visual and qualitatively comparison of the Raman and the Photoluminescence results. For the Raman: good is a sample without the "shoulder", in other words, without the OVC phase; mixed is a sample which has the OVC phase appearance in some measurements; and bad is a sample with the OVC phase present in almost all the measurements. For the PL it was considered good, a sample with only one narrow peak; mixed, a sample with one broader peak; and bad, a sample with more than one peak.

In summary, the samples with good results so far are the B - SiO_x - 150 °C, HF and LF. The A – Al_2O_3 - ALD sample, although lacking the PL results, is expected to be one of the samples that does not cause damage to the CIGS surface as well, because did not have the OVC phase in the Raman analysis. It is clear that the sputtering damages the CIGS surface (Al_2O_3 deposited by sputtering sample) in addition to the high temperatures (SiO_x deposited by PECVD at 300 °C, HF sample) and such damage causes the OVC phase appearance in the Raman measurements and more than one peak, as well as, broader peaks in the PL results. Unexpectedly, the A - Si_3N_x sample did not show good results due to the presence of the OVC phase in the Raman analysis and the presence of two peaks in PL. Since the deposition method was the same as the one deposited with B - SiO_x – 150 ºC, HF, with the difference of the precursor gases used, must be an indication that the temperature, frequency and plasma power used in the deposition should not affect the CIGS layer. However, the only difference is the use of ammonia (NH_3) in the Si_3N_x deposition instead of nitrous oxide (N_2O) of the SiO_x deposition. This difference, can be an indication that the ammonia gas is affecting the CIGS surface layer.

Table 3 - Comparison between Raman spectroscopy and Photoluminescence measurements using a qualitatively three-degree comparison: good, mixed and bad.

	Raman spectroscopy	Photoluminescence
A - CdS	Good	Good
A - Al_2O_3 - S	Bad	Bad
A - Si_3N_x	Bad	Bad
A - Al_2O_3 - ALD	Good	Not measured
B - CdS	Good	Good
B - SiO_x - 300 °C	Bad	Bad
B - SiO_x - 150 °C, HF	Mixed	Good
B - SiO_x - 150 °C, LF	Mixed	Good

3.6. Electrical measurements

In this chapter, several electrical measurements done to the MIS structures will be presented in order to understand the electrical performance of the CIGS/insulator interface. One of the samples with several MIS structures is depicted in **Figure 3.5**.

The electrical measurements in this chapter aims to reach the fixed insulator charges (Q_f) and the density of interface defects (D_{it}) in the CIGS/insulator interface. Before the measurements, several fittings were done to the MIS structures in order to understand the most suitable method and model to be used in the Q_f and D_{it} values calculation.

Figure 3.5 - Representative sample with MIS structures having several metal diameters, namely 1 mm, 2 mm and 3 mm.

In the literature, several studies show how to accomplish the fixed insulator charges using MIS structures [22,37,39–41]. While most of these works are for standard semiconductors like Si and GaAs, for CIGS there is only one paper, and there, the exact measurement conditions are not explained [41]. However, most of the authors [22,39–41] always take in consideration that the MIS structure is represented by the equivalent circuit models depicted in **Figure 1.6**.

In order to understand the models' accuracy shown in **Figure 1.6**, and taking into account real MIS structures, fittings to the MIS's models were done using the ZSimpWin 3.50 software. The main focus of this study was to understand if the models presented are related to the current measurements and to identify if shunts are present in the insulator.

C-G-f measurements were carried out in the Agilent E4890 A, being the equivalent circuit represented in **Figure 1.6 c)** considered by default. In order to use the ZSimpWin 3.50 software, the input data should be the frequency, as well as, the real and imaginary parts of the circuit's impedance, Z' and Z'' respectively. Thus, it is needed to know the impedance of the measured equivalent circuit, in this case, a resistance in parallel with a capacitance. The impedance of this parallel circuit is represented by:

$$Z = \frac{jRX}{R + jX} = \frac{RX^2}{R^2 + X^2} + j\frac{R^2X}{R^2 + X^2} \tag{9}$$

where R is the resistance and X is the reactance. The impedances' real and imaginary parts are, respectively, given by:

$$Z' = \frac{RX^2}{R^2 + X^2} \tag{10}$$

and

$$Z'' = \frac{R^2X}{R^2 + X^2} \tag{11}$$

The X is the reactance, and in this case, it is only defined by the capacitance, becoming:

$$X = X_C = \frac{1}{2\pi fC} = \frac{1}{\omega C} \tag{12}$$

where f is the frequency, ω is the angular frequency and C is the capacitance.

After the device's extracted values being converted to impedance, several fittings were done to every MIS structure of each sample accounting to more than 140 measurements in total. To represent the insulator branch, a constant phase element (CPE) was used, that is an equivalent electrical circuit component that models the behaviour of an imperfect capacitor. The CPE impedance is represented by the following equation:

$$Z = \frac{1}{Q_0(j\omega)^n} \tag{13}$$

where ω is the angular frequency, the Q_0 has the numerical value of the admittance ($1/|Z|$) at $\omega = 1$ rad/s and the value n is between 0 (pure resistance) and 1 (pure capacitor).

By using the CPE element in the fittings to represent the insulator branch, it was possible to comprehend if we can consider that the branch is represented only by a capacitor, which is the best-case scenario, or if the branch has a high resistance component, in this case it is safe to assume that a shunt is present. For the sake of comparison between the samples, n values above 0.8 are considered pure capacitors and below are considered shunts [58].

A graphical representation of the study is shown in **Figure 3.6**, where all the samples are present, using a qualitatively three-degree comparison: green, yellow and red. Dots that are coloured in green correspond to MIS structures where an insulator can be electrically represented as a pure capacitor; the red means an insulator mostly dominated by a resistive behaviour, thus, the sample is assumed to be shunted; and yellow means that the value n is close to 0.8. In these dubious cases we assume these measurements are inconclusive.

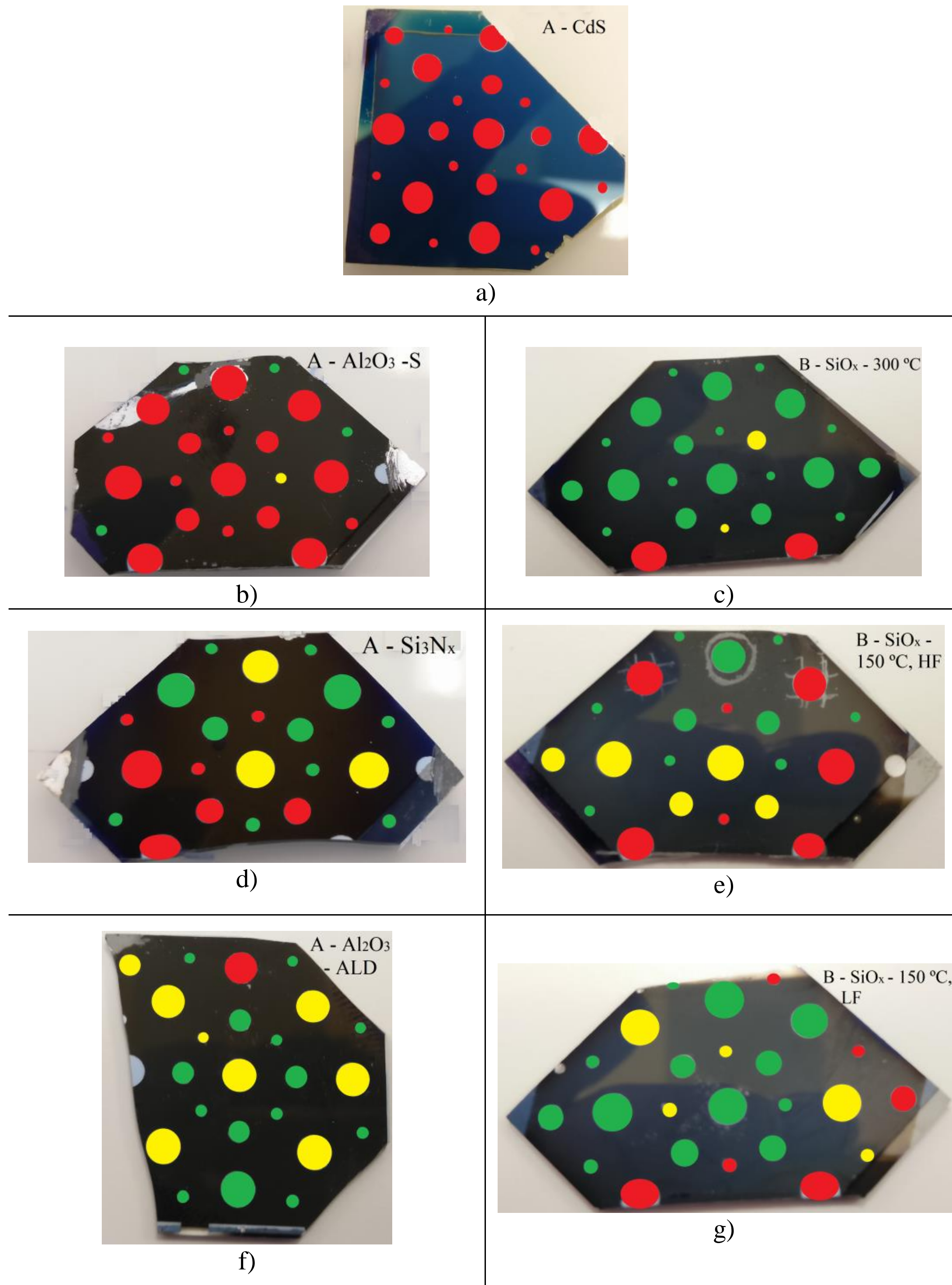

Figure 3.6 – MIS structures using a qualitatively three-degree comparison: good (green), mixed (yellow) and bad (red). CIGS A in the left side and CIGS B in the right side. A) A – CdS; b) A- Al_2O_3 – S; c) B - SiO_x - 300 ºC; d) A - Si_3N_x; e) B - SiO_x - 150 ºC, HF; f) A - Al_2O_3 - ALD; and g) B - SiO_x - 150 ºC, LF.

Before the study discussion, it is necessary to understand that a shunt is more likely to be present for higher front contact area diameters. Thus, the 3 mm MIS structures have more probability of having shunts.

The A – CdS reference sample is shown in **Figure 3.6 a)**, where all the structures are red, meaning their electrical behaviour is not dominated by a capacitance as expected in an ideal MIS. Consequently,

one can conclude the same to the B – CdS sample. This result was expected, due to no insulator deposition was done. These samples do not form a MIS structure and, in fact, a CdS layer is deposited on top of the CIGS layer.

Considering the CIGS piece A, the most damaged sample is the A – Al_2O_3 – S sample, shown in **Figure 3.6 b)**. Only a few structures of 1 mm survived, more precisely 40 % of them. In **Figure 3.6 d)**, the A – Si_3N_x sample is present. As it is depicted, 75 % of the 1 mm MIS structures, 50 % of the 2 mm structures and 25 % of the 3 mm structures are working as an ideal MIS. This is a good demonstration that more shunts are likely to be present for higher front metal areas. The sample A – Al_2O_3 – ALD, depicted in **Figure 3.6 f)** was the most difficult sample to study. The yellow MIS structures shown in this figure for the 3 mm MIS structures have shown high fitting errors values, i.e. some capacitance values in the fittings had error values above 10^{13} % for the model used. Consequently, more complex models should be fitted in order to accomplish lower errors values, and, therefore, to get more accurate conclusions. Due to be time-consuming, more complex models were not tested and the MIS structures were considered inconclusive.

For the CIGS piece B, the sample B – SiO_x – 300 ºC is depicted in **Figure 3.6 c)**. Almost all the MIS structures are behaving as ideal MIS strictures, with the capacitance's component dominating, which is the best result so far. It is shown in **Figure 3.6 e)**, the B - SiO_x – 150 ºC, HF sample. As it is represented, 76 % of the 1 mm MIS structures, 40 % of the 2 mm structures and 16 % of the 3 mm have a stronger capacitance's component. Lastly, in **Figure 3.6 g)**, the B - SiO_x – 150 ºC, LF sample is shown, and contrarily to previous results, most of the shunted structures are the 1 mm ones. 40 % of the 1 mm MIS structures, 83 % of 2 mm structures and 66 % of 3 mm structures have a stronger capacitance component.

To recapitulate all the information, a summary of the results is shown in **Table 4**, with the percentage of the MIS structures without shunts. The red colour means a sample almost only with shunts; the yellow colour means a mixed sample with both shunted and not shunted MIS structures; and a green colour means a sample almost without shunts. The light green colour refers to the inconclusive measured sample.

Table 4 - Comparison between the samples, taking into account the metal diameter using the percentage of non-shunted structures and qualitatively three-degree overall comparison: good (green), mixed (yellow) and bad (red).

	1 mm (%)	2 mm (%)	3 mm (%)
A - CdS	0	0	0
A - Al_2O_3 - S	40	0	0
A - Si_3N_x	75	50	25
A - Al_2O_3 - ALD	90	80	inconclusive
B - SiO_x - 300 °C	90	83	100
B - SiO_x - 150 °C, HF	75	40	16
B - SiO_x - 150 °C, LF	40	83	66

As shown in **Table 4**, samples with fewer shunts are the B - SiO_x - 300 °C and the B - SiO_x - 150 °C, LF. The A - Al_2O_3 – ALD sample, while not conclusive taking into account the model used for the 3 mm MIS structures, it can also be considered a sample with most of the MIS structures behaving like an ideal MIS.

After the study of the shunted samples, the fixed insulator charges and the density of the interface defects in the CIGS/insulator interface will be studied. Only the MIS structures considered good and mixed will be measured. At the end, a summary will be presented, to understand the correlation between all the measurements.

3.6.1 *Fixed insulator charges (Q_f)*

Numerous types of charges can be present in the insulator, namely the fixed insulator charges (Q_f), the mobile ionic charges (Q_m) and the insulator trapped charges (Q_{ot}). In this chapter, only the fixed

insulator charges will be discussed due to be the ones contributing to the field-effect passivation. Taking into account that the polarity of the fixed charges in the insulator are of utmost importance, since the front contact and the rear contact passivation should have positive and negative polarity charges respectively, for the optimum field-effect passivation [26], the Q_f calculation is an imperative measurement. The fixed insulator charges are physically represented in **Figure 6.5** of **Annexes.**

Several calculations will be shown in this chapter. Before that, some notions should be presented in order to understand the physical concepts behind the calculations and models used. Considering an ideal MIS structure, the related C-V curve is depicted in **Figure 6.6**, where the flat-band voltage is assumed to be 0V, thus, the depletion region can be considered in the region of the C-V curve's slope, near 0V. However, in real MIS structures, the flat-band voltage is not 0V and, consequently, the depletion region is not near 0V, as well. The reason for the shift in the flat-band voltage is directly related with the fixed insulator charges, as it is shown in **Figure 6.7**. A shift in the C-V curve also happens with the value ΔV (flat-band voltage) and the direction of the shift depends on the polarity of the insulator charges [40]. A positive insulator charge (+Q) will require a more negative applied voltage so that the flat-band condition can be reached. The contrary effect is expected if the insulator charges are negative (-Q) as it is depicted in **Figure 3.7**.

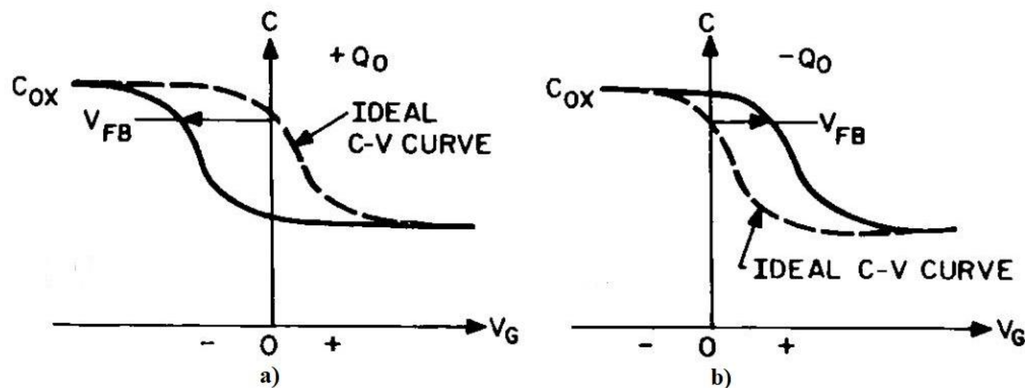

Figure 3.7 - Shift in C-V curve due to fixed insulator charges in a p-type semiconductor. a) Positive insulator charges effect; b) Negative insulator charges effect. Adapted from [39].

The calculation of the fixed insulator charges is done using equation (4).

C_{in} will be calculated through the C-V curves in strong accumulation, the CIGS/Al work function is equal to -0.97V [41] and the flat-band voltage will be calculated through the graphical method explained before.

A representative C-V curve is shown in **Figure 3.8** and it looks like the expected curve shown in **Figure 6.6 c)**. More than 140 C-V measurements were carried out in order to extract all the necessary information of each MIS structure. Therefore, it is not possible to show all the measured graphs and a representative one is shown.

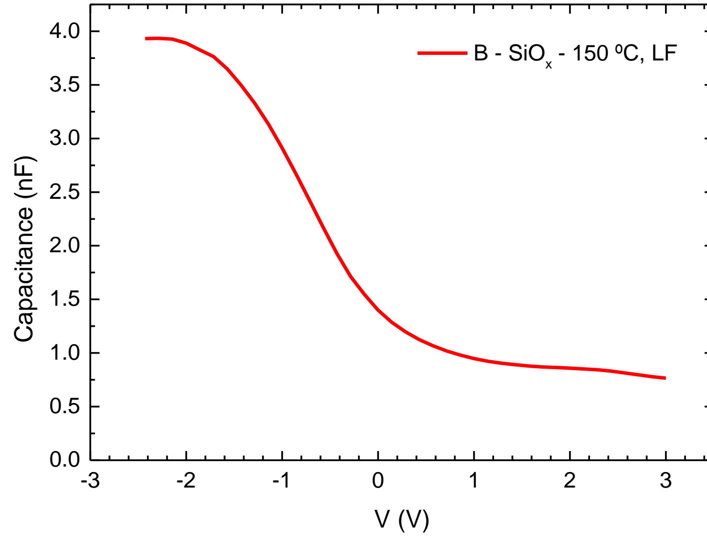

Figure 3.8 - Representative C-V curve. Sample B – SiO_x – 150 ºC, LF. MIS with 2 mm.

As shown in **Figure 3.8**, looking to the strong accumulation part (the most negative bias), the C_{in} value can be extracted, being in this case, equal to 3.9 nF. A summary of all extracted C_{in} average and standard deviation values for each diameter of each sample are shown in **Table 5**.

Table 5 – C_{in} average and standard deviation values of each diameter for each sample.

C_{in} (F)	A - Al_2O_3 - S	A - Si_3N_x	A - Al_2O_3 - ALD	B - SiO_x - 300 °C	B - SiO_x - 150 °C, HF	B - SiO_x - 150 °C, LF
1 mm	$(7.2 \pm 2.8) \times 10^{-10}$	$(4.1 \pm 2.2) \times 10^{-10}$	$(9.0 \pm 0.9) \times 10^{-10}$	$(5.3 \pm 0.8) \times 10^{-10}$	$(5.4 \pm 2.8) \times 10^{-10}$	$(7.8 \pm 1.6) \times 10^{-10}$
2 mm	4.9×10^{-9}	2.0×10^{-9}	$(3.1 \pm 0.09) \times 10^{-9}$	2.2×10^{-9}	$(3.6 \pm 0.2) \times 10^{-9}$	$(3.7 \pm 0.2) \times 10^{-10}$
3 mm	$(7.4 \pm 3.9) \times 10^{-9}$	$(6.3 \pm 3.2) \times 10^{-9}$	$(7.8 \pm 1.7) \times 10^{-9}$	$(5.5 \pm 0.2) \times 10^{-9}$	$(6.2 \pm 2.4) \times 10^{-9}$	$(8.2 \pm 1.6) \times 10^{-9}$

It is noted that some C-V curves just had the beginning of the slope and not the end of it, thus, in these cases, it was not possible to extract the C_{in}, as it is visible in the samples without standard deviation, namely the 2 mm MIS structures of the samples A - Al_2O_3 – S, A - Si_3N_x and B - SiO_x - 300 °C. The potential (V) range used for each diameter of each sample was different in order for the slope to be present. Nevertheless, it was not always possible to accomplish the desired curve, even trying with higher ranges, since in the extreme of this range the values were too high or too low for the device.

The samples without standard deviation have C_{in} values following the same trending of the other samples, i.e. all the three are for 2 mm MIS structures with: C_{in} values for 1 mm always lower and for 3 mm always higher (it is expected that the C_{in} increases with the diameter).

The flat-band voltage was extracted, using the graphical method, following the equation presented next [38]:

$$\left(\frac{C_{in}}{C_m}\right)^2 - 1 = 0 \tag{14}$$

where the C_{in} is the capacitance value in strong accumulation and the C_m is the measured capacitance.

A representative graph of the flat-band voltage (V_{fb}) extraction is shown in **Figure 3.9**.

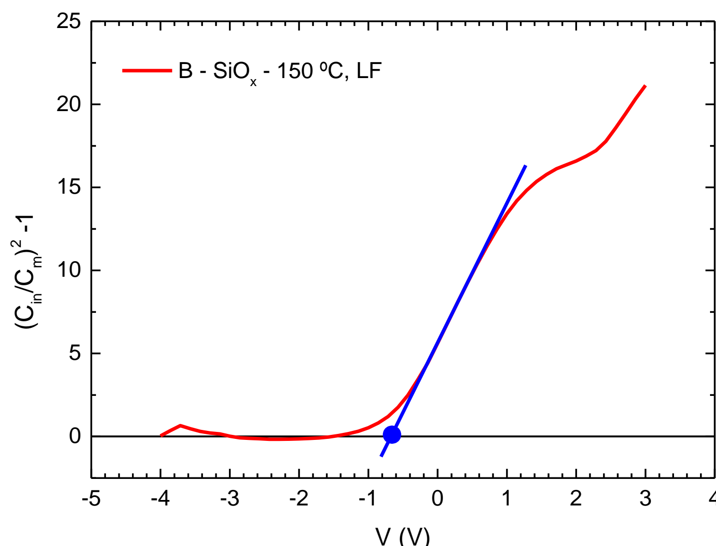

Figure 3.9 - Representative V_{fb} calculation through the graphical method. Sample B – SiO_x – 150 ºC, LF. MIS with 2 mm.

In **Figure 3.9**, it is shown the same sample used before for the C_{in} calculation in **Figure 3.8**. The V_{fb} value is equal to -0.66 V in this case and a summary of all extracted average and standard deviation V_{fb} values are shown in **Table 6**.

Table 6 – V_{fb} average and standard deviation values of each diameter for each sample.

V_{fb} (V)	A - Al_2O_3 - S	A - Si_3N_x	A - Al_2O_3 - ALD	B - SiO_x - 300 °C	B - SiO_x - 150 °C, HF	B - SiO_x - 150 °C, LF
1 mm	-1.6 ± 0.7	-2.0 ± 1.2	-1.5 ± 0.4	-1.9 ± 0.3	-1.6 ± 0.4	-0.9 ± 0.2
2 mm	-0.8 ± 0.7	+2.7 ± 1.2	-1.5 ± 0.03	-2.0 ± 0.0	-2.0 ± 0.1	-0.9 ± 0.3
3 mm	-1.1 ± 0.2	0.0 ± 0.4	-1.7 ± 0.2	-0.9 ± 0.1	-2.0 ± 0.2	-0.8 ± 0.1

From now on, we have all the necessary values for the Q_f calculation. It is necessary to understand that just by looking to the C-V curves, it is not possible to take any conclusions about the polarity of the fixed insulator charges. However, taking into account the equation (4), the only variable parameter is the V_{fb}, thus, knowing the CIGS/Al work function (W_{ms}), it is possible to predict the charge polarity. If the V_{fb} is more negative than the W_{ms}, then the charges will be negative, otherwise the charges will be positive.

The Q_f was calculated for each sample's diameter, considering the average values of the C_{in} and V_{fb} calculated previously. Considering the equation (4), all the Q_f values are shown in **Table 7**.

Table 7 – Q_f values taking into account the average C_{in} and V_{fb} calculated before. The red samples have negative charges in the insulator.

Q_f (cm^{-2})	A - Al_2O_3 - S	A - Si_3N_x	A - Al_2O_3 - ALD	B - SiO_x - 300 °C	B - SiO_x - 150 °C, HF	B - SiO_x - 150 °C, LF
1 mm	$+3.6 \times 10^{11}$	$+3.2 \times 10^{11}$	$+4.1 \times 10^{11}$	$+4.0 \times 10^{11}$	$+2.8 \times 10^{11}$	-6.1×10^{10}
2 mm	-2.1×10^{11}	-1.5×10^{12}	$+3.1 \times 10^{11}$	$+4.5 \times 10^{11}$	$+7.5 \times 10^{11}$	-8.4×10^{10}
3 mm	$+8.4 \times 10^{10}$	-5.4×10^{11}	$+4.9 \times 10^{11}$	-5.5×10^{11}	$+6.1 \times 10^{11}$	-1.4×10^{11}

As shown in **Table 7**, the most uniform samples are the A - Al_2O_3 – ALD, the B - SiO_x - 150 °C, HF and the B - SiO_x - 150 °C, LF. The A - Al_2O_3 – ALD and B - SiO_x - 150 °C samples have positive charges contrary to B - SiO_x - 150 °C, LF sample, having negative insulator charges. The only difference between the B - SiO_x - 150 °C, HF and the B - SiO_x - 150 °C, LF samples, is the plasma frequency of the deposition, which according to these results causes a change in the fixed insulator charges polarity. This is exactly the reason why two different deposition conditions were tested as it is known they greatly

influence the insulator properties. Considering the A - Al_2O_3 - ALD sample, the results are in agreement with R. Kotipalli *et al.* [41] which calculated the Q_f values for Al_2O_3 deposited by ALD with a metal front contact of approximately 1 mm. In their case, for the as-deposited (without annealing) sample, they reached Q_f values in the magnitude of 10^{11} and with positive polarities.

The A - Al_2O_3 - S, the A - Si_3N_x and the B – SiO_x – 300 ºC samples are inhomogeneous. They show both positive and negative insulator charges. In order to understand if a preferential position of the samples have the different polarities of the fixed insulator charges, all the values of the calculated Q_f were positioned with the corresponding MIS structure in the sample. However, no correlation between the position and the Q_f was found. Thus, the polarity of the charges is not correlated with the insulator deposition.

The density of interface defects results will be discussed in the next chapter and a summary of all the measured techniques will be presented as well in the end of it.

3.6.2 *Density of interface defects (D_{it})*

This chapter aims to relate the measured admittance of the MIS structures with values of interface trap density (D_{it}). The admittance is not taken directly from the measurements, but it can be extracted using an equivalent model, as shown in **Figure 1.6**. The interface defects are physically represented in **Figure 6.5** of **Annexes**.

There are two methods that can be used to extract the density of interface defects [39,40]: the conductance or the capacitance method. The conductance method is more accurate and sensitive [39, 40], being the method used in this master thesis. In order to apply the conductance method, C-G-f measurements were done. The parallel capacitance C_m and the parallel conductance G_m are extracted from the equipment taking into account the equivalent circuit presented in **Figure 1.6 c)**. The admittance of the MIS structure measured is $G_m + j\omega C_m$. This admittance can be converted to the conductance of the interface-trap branch, as it is shown in equation (8) [22,39,40].

The equation yields at a peak maximum $\left(\frac{G_p}{\omega}\right)_m$ corresponding to the energy loss at the interface due to the trapping and de-trapping mechanisms. It is noted that the measurement should be carried out at a voltage near flat-band [22,39], thus, taking into account **Table 6**, each diameter of each sample was measured at different voltages.

One representative $\frac{G_p}{\omega}$ curve is shown in **Figure 3.10**. As it was said before, several measurements were carried out to all MIS diameters of each sample, and only a representative curve is shown here.

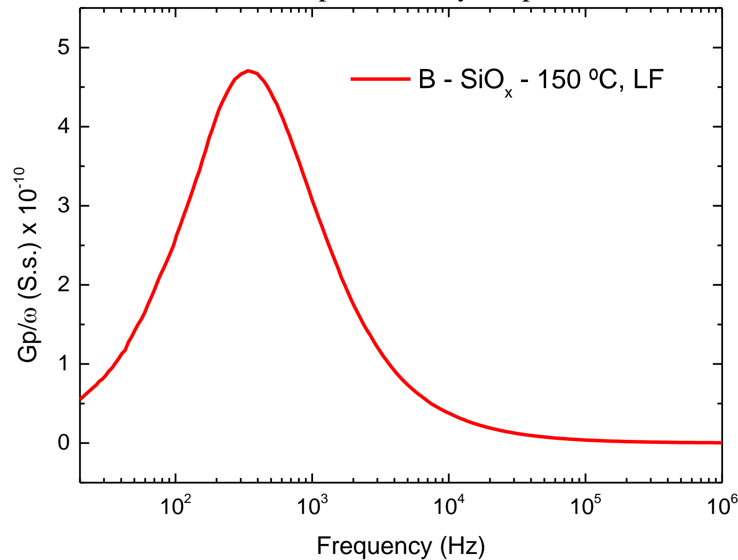

Figure 3.10 - C-V representative curve of sample B – SiO_x – 150 ºC, LF. MIS with 2 mm.

In the case of **Figure 3.10**, the maximum peak value is 4.7x10^{-10} S.s., consequently, applying the equation (7), the D_{it} value is 9.9x10^{11} $eV^{-1}cm^{-2}$. In **Table 8**, the D_{it} average and standard deviation values of each diameter for each sample is shown.

Table 8 - D_{it} average and standard deviation values of each diameter for each sample.

D_{it} (eV^{-1} cm^{-2})	A - Al_2O_3 - S	A - Si_3N_x	A - Al_2O_3 - ALD	B - SiO_x - 300 °C	B - SiO_x - 150 °C, HF	B - SiO_x - 150 °C, LF
1 mm	$(7.6 \pm 0.3) \times 10^{11}$	$(1.6 \pm 1.0) \times 10^{12}$	$(3.8 \pm 1.4) \times 10^{12}$	$(3.1 \pm 1.9) \times 10^{12}$	$(5.7 \pm 3.2) \times 10^{12}$	$(2.3 \pm 3.0) \times 10^{12}$
2 mm	shunted	$(7.2 \pm 0.3) \times 10^{11}$	inconclusive	$(5.9 \pm 0.3) \times 10^{11}$	$(1.0 \pm 0.6) \times 10^{13}$	$(1.2 \pm 0.3) \times 10^{12}$
3 mm	shunted	$(1.6 \pm 0.4) \times 10^{12}$	inconclusive	$(7.6 \pm 1.5) \times 10^{11}$	$(6.1 \pm 0.6) \times 10^{12}$	$(1.2 \pm 0.1) \times 10^{12}$

It is noted that only the MIS structures with a strong capacitance component in the insulator branch were measured, considering the shunt study, presented in the beginning of chapter **3.6**. As shown in **Table 8**, the A - Al_2O_3 – S sample has most of the MIS structures shunted, thus, it was only possible to calculate the density of interface defects for the 1 mm structures. The A - Al_2O_3 – ALD sample is inconclusive for the 2 and 3 mm MIS structures due to a presence of a double peak. In the shunts study, it was also inconclusive for the 3 mm MIS structures. The explanation was that the model used for the fittings, and consequently for the conductance method measurement, is not the most suitable model. In order to calculate the D_{it}, it is necessary to accomplish the most suitable model for this sample, and, thus, achieve a new equation to replace the equation (8). Nevertheless, accordingly to R. Kotipalli *et al.* [41] the calculated D_{it} values were in the magnitude of 10^{12} for the Al_2O_3 deposited by ALD insulator (as-deposited) with a metal front contact of approximately 1 mm, which is in agreement with our measurements. Also, accordingly to [59], the maximum acceptable limit for the D_{it} is 1×10^{13} in order for the passivation effect to be positive and none of the presented samples have D_{it} values higher than 1×10^{13} indicating that the passivation layer is working, thus, an high electrical performance should be present.

3.7. Summary

All the measured results are summarized in **Table 9**.

Table 9 - Summary of all used techniques. Qualitatively three-degree overall comparison: good, mixed and bad. The Q_f measurement has different colours due to not be possible to do a qualitatively comparison.

	Raman spectroscopy	Photoluminescence	Shunts	Q_f
A - Al_2O_3 - S	Bad	Bad	Yes	Mixed charges
A - Si_3N_x	Bad	Bad	Mixed	Mixed charges
A - Al_2O_3 - ALD	Good	Not measured	Inconclusive	Positive charges
B - SiO_x - 300 °C	Bad	Bad	No	Mixed charges
B - SiO_x - 150 °C, HF	Mixed	Good	Mixed	Positive charges
B - SiO_x - 150 °C, LF	Mixed	Good	No	Negative charges

Taking into consideration all of the measurements, shown in **Table 9**, the A – Al_2O_3 – S sample is the one least promising to be used as passivation layer. The CIGS film quality measurements indicate a surface damage on CIGS and the passivation layer electrically have more shunts. On the other hand, the B - SiO_x - 150 °C, LF sample has the most promising results, since it does not have surface CIGS damage and does not have shunts.

The B – SiO_x – 300 °C sample has damaged CIGS surface, as expected, taking into account the high values of temperature involved in the insulator deposition. However, this sample is the one with no shunts, although the polarity of the charges is not clear. The insulator deposition damages the CIGS, but the insulator appears to be of good quality since it has no electrical shunts. Considering these results, the B – SiO_x – 300 °C insulator should be more suitable for the rear contact passivation, instead of the front contact, since no CIGS is under it, just molybdenum.

The B - SiO_x - 150 °C, HF have almost the same results as the B - SiO_x - 150 °C, LF, though with more shunts. However, it is a quite positive result, taking into consideration that the only big difference is the polarity of the charges. The B - SiO_x - 150 °C, HF, since it has positive charges, is more suitable for the front contact and the B - SiO_x - 150 °C, LF, with negative charges is more suitable for the rear contact, in relation to the field-effect passivation.

The A - Si_3N_x sample damages the CIGS surface and at the same time it is difficult to take any conclusions, considering the mixed results of the electrical experiments which by itself is an indication of lack of uniformity and it might reveal that the growth of the layer is not done properly on CIGS.

The A - Al_2O_3 – ALD, being successfully used as passivation layer in the silicon technology, it is promising to be used in other solar cell technologies as well. However, without the PL results and with the lack of information about the electrical measurements, it is difficult to reach a clear conclusion. It is required more measurements to understand the CIGS damage and more tests with the electrical measurements, namely the use of more complex models for the fittings and density of interface defects calculation.

4 Conclusion and Future Perspectives

The main focus of this master thesis was the study of the influence of the insulator and of the deposition conditions on the CIGS surface to be effectively used as a passivation layer.

The measurements done to quantify the insulator deposition influence have shown that the insulator B - SiO_x - 150 ºC, both LF and HF are the ones that likely impose less CIGS surface damage as shown by Raman and Photoluminescence measurements. The A - Al_2O_3 - ALD sample, has shown good Raman spectroscopy results that are an indication of a CIGS surface undamaged by the insulator deposition. The A - Al_2O_3 - S, the B - SiO_x - 300 ºC and the A - Si_3N_x have clear indications that its deposition process damages the CIGS surface as it is shown by the Raman and Photoluminescence measurements. The reason for the poor results, in the A - Al_2O_3 – S case, is the deposition method, sputtering, that with some material depositions, it is well known to cause damage on CIGS, however in the Al_2O_3 case it was not studied before, being now proven to damage as well. In the B - SiO_x - 300 ºC sample, the high temperatures involved in the deposition process are known to damage the CIGS in certain conditions, namely annealing with air exposure or in selenium. However, in vacuum and more precisely using the SPTS MPX CVD tool it was not known, being now proven to also damage the CIGS surface. In the A - Si_3N_x case, the only difference with the B - SiO_x - 150 ºC, HF was the precursor gases used in the deposition, namely the ammonia (NH_3), which can be the reason for the CIGS surface damage.

The X-ray diffraction, since it is a bulker measurement technique than Raman spectroscopy, did not shown any differences between the samples, meaning that some of the CIGS had shallow damage and not bulk ones.

The study of the relation between the MIS structure and the correct model to define it has shown that the A - Al_2O_3 - S sample is the one with more shunts, thus, having the insulator branch a dominant resistive component. These results can be explained by the non-conformal growth of the Al_2O_3 layer, thus, more pinholes are present and, consequently, more shunts. The A - Si_3N_x and the B - SiO_x - 150 ºC, HF samples, have a mix between MIS structures with a dominant capacitive component and a dominant resistive component. The A - Al_2O_3 - ALD sample, for 1 mm and 2 mm MIS diameters has shown good results, however, for 3 mm, the results are inconclusive. The results did not show shunts, although the error applying the models were high, thus, more complex models/circuit modes should be applied to understand which models are suitable for the 3 mm A - Al_2O_3 - ALD case. The B - SiO_x - 300 ºC and the B - SiO_x - 150 ºC, LF samples are the ones with less shunts, thus, the MIS structures can be represented by the models presented in **Figure 1.6**. The study of shunts is important to validate other electrical measurements and furthermore, in a real solar cell device, a low number of shunts will be wanted.

The study of the fixed insulator charges has shown that the A - Al_2O_3 - S, the A - Si_3N_x and the B - SiO_x - 300 ºC samples have both positive and negative fixed charges. A correlation between the mixed charges and both the Raman spectroscopy and Photoluminescence poor result exists, as it was shown in **Table 9**. The A - Al_2O_3 – ALD and the B - SiO_x - 150 ºC, HF have positive fixed charges and the B - SiO_x - 150 ºC, LF have negative fixed charges. The identification of materials and deposition conditions with positive and negative charges was important, since it can allow for both rear and front interface passivation.

In summary, the A - Al_2O_3 – S and the A - Si_3N_x are materials that are not likely to be good as passivation materials for CIGS solar cells. The A - Al_2O_3 – ALD sample does not damage the CIGS surface and at the same time appears to have a good interface electrical performance, however, more measurements are needed, namely the PL measurement and more fittings to better understand the right model to be used in the density of interface defects calculation. The fixed insulator charges study has shown positive charges inside this insulator, hence, it should be used as the front passivation layer. The B – SiO_x – 300 ºC deposition damaged the CIGS surface, though the electrical measurements were good, being one of the sample with less shunts. We attribute the lack of shuts to the superior deposition conditions of the insulator itself that the high temperature allows for. Since the CIGS surface was damaged, more studies should be carried out, in order to understand the behaviour of the B – SiO_x – 300 ºC sample on the rear contact. If the surface damage is not present, then it could be used as rear passivation layer.

Both B - SiO_x - 150 ºC, LF and HF samples have not damaged completely the CIGS surface and the electrical measurements were good with a particularity: the HF sample has shown positive fixed charges and the LF sample has shown negative fixed charges. The change in the polarity of the charges are due to the frequency of the PECVD deposition, which means that, just by varying the frequency, one can have a good passivation layer for the front contact (B - SiO_x - 150 ºC, HF) or a good passivation layer for the rear contact (B - SiO_x - 150 ºC, LF). Again, in order to understand the behaviour of the B - SiO_x - 150 ºC, LF sample on the rear contact, more studies should be carried out. This result is the most promising result of this work as it opens the door to passivation of both CIGS interfaces using the same material.

Despite the number of fixed charges inside the insulator or the polarity of them contributing to the field-effect passivation, it is important to remember that the chemical passivation is also present, causing a decrease in the number of active defects than without the passivation layer. Therefore, even with lower concentration of fixed insulator charges or with mixed charges in it, it is expected an increase in the performance of the device due to the chemical passivation.

The density of interface defects measurements do not allow us to take any conclusions about differences between the samples. However, the maximum acceptable limit for the values of D_{it} is 1×10^{13} [59], and all the measured samples have lower D_{it} values. An important identification of the literature search done in this work has also shown that in the literature a consensual value for the D_{it} determined experimentally is not available.

As future perspectives, more complex models should be used in order to accomplish more precise results in the shunts study and to reach an equation more accurate to calculate the density of interface defects. An annealing should be done to the samples, since the annealing process after the insulator deposition changes the insulator properties [41], namely the polarity of the fixed insulator charges, which can allow us to use the same insulator in both front and rear passivation. The D_{it} measurements should be done at different temperatures, considering that the behaviour of the interface defects changes with temperature. Finally, complete solar cells with the more promising layers, i.e. SiO_x deposited by PECVD at 150 ºC, HF and Al_2O_3 deposited by ALD for the front contact and SiO_x deposited by PECVD at 150 ºC, LF for the rear contact should be done, since the objective of this master thesis, the study of the most promising insulator materials to serve as passivation layer on solar cells, was accomplished.

A paper is being prepared to be submitted with the results of this master thesis.

5 Bibliography

[1] W. Shockley and H. J. Queisser, "Detailed balance limit of efficiency of p-n junction solar cells" *J. Appl. Phys.*, vol. 32, no. 3, pp. 510–519, 1961.

[2] M. A. Green, "The Passivated Emitter and Rear Cell (PERC): From conception to mass production" *Sol. Energy Mater. Sol. Cells*, vol. 143, pp. 190–197, 2015.

[3] M. Kemell, M. Ritala, and M. Leskelä, "Thin Film Deposition Methods for $CuInSe_2$ Solar Cells" *Crit. Rev. Solid State Mater. Sci.*, vol. 30, no. 1, pp. 1–31, 2005.

[4] L. Fraas and L. Partain, Eds., *Solar Cells and their Applications*. Hoboken, NJ, USA: John Wiley & Sons, Inc., 2010.

[5] V. Fthenakis, "Sustainability of photovoltaics : The case for thin-film solar cells" vol. 13, pp. 2746–2750, 2009.

[6] M. A. Green, Y. Hishikawa, W. Warta, E. D. Dunlop, D. H. Levi, J. Hohl-Ebinger, and A. W. H. Ho-Baillie, "Solar cell efficiency tables (version 50)" *Prog. Photovoltaics Res. Appl.*, vol. 25, no. 7, pp. 668–676, Jul. 2017.

[7] R. Kamada, T. Yagioka, S. Adachi, A. Handa, K. F. Tai, T. Kato, and H. Sugimoto, "New World Record Cu(In,Ga)$(Se,S)_2$ Thin Film Solar Cell Efficiency Beyond 22%" in *2016 IEEE 43rd Photovoltaic Specialists Conference (PVSC)*, 2016, pp. 1287–1291.

[8] IRENA, "Solar Photovoltaics" 2012.

[9] P. Salomé, "Chalcogenide Thin Films for Solar Cells: Growth and Properties" University of Aveiro, 2011.

[10] M. A. Green, "Solar cell fill factors: General graph and empirical expressions" *Solid. State. Electron.*, vol. 24, no. 8, pp. 788–789, Aug. 1981.

[11] F. Mollica, "Optimization of ultra-thin Cu(In,Ga)Se_2 based solar cells with alternative back-contacts" Université Pierre et Marie Curie - Paris VI, 2016.

[12] A. M. Humada, M. Hojabri, S. Mekhilef, and H. M. Hamada, "Solar cell parameters extraction based on single and double-diode models : A review" *Renew. Sustain. Energy Rev.*, vol. 56, pp. 494–509, 2016.

[13] W. Shockley, "Electrons and Holes in Semiconductors." 1950.

[14] P. M. P. Salomé, H. Rodriguez-alvarez, and S. Sadewasser, "Solar Energy Materials & Solar Cells Incorporation of alkali metals in chalcogenide solar cells" *Sol. Energy Mater. Sol. Cells*, vol. 143, pp. 9–20, 2015.

[15] N. Severino, N. Bednar, and N. Adamovic, "Buffer layer optimization for high efficiency CIGS solar cells" *J. Phys. Conf. Ser.*, vol. 758, p. 12016, Oct. 2016.

[16] B. J. Stanbery, "Copper Indium Selenides and Related Materials for Photovoltaic Devices" *Crit. Rev. Solid State Mater. Sci.*, vol. 27, 2002.

[17] K. Gartsman, L. Chernyak, V. Lyahovitskaya, D. Cahen, V. Didik, V. Kozlovsky, R. Malkovich, E. Skoryatina, and V. Usacheva, "Direct evidence for diffusion and electromigration of Cu in $CuInSe_2$" *J. Appl. Phys.*, vol. 82, 1997.

[18] B. Vermang, V. Fjällström, J. Pettersson, P. Salomé, and M. Edoff, "Development of rear surface passivated Cu(In,Ga)Se_2 thin film solar cells with nano-sized local rear point contacts" *Sol. Energy Mater. Sol. Cells*, vol. 117, pp. 505–511, 2013.

[19] J. E. Jaffe and A. Zunger, "Electronic structure of the ternary chalcopyrite semiconductors $CuAlS_2$, $CuGaS_2$, $CuInS_2$, $CuAlSe_2$, $CuGaSe_2$, and $CuInSe_2$" *Phys. Rev. B*, vol. 28, no. 10, 1983.

[20] J. Kessler, C. Chityuttakan, J. Lu, J. Schöldström, and L. Stolt, "Cu(In,Ga)Se_2 thin films grown with a Cu-poor/rich/poor sequence: growth model and structural considerations" *Prog. Photovoltaics Res. Appl.*, vol. 11, no. 5, pp. 319–331, Aug. 2003.

[21] J. L. Shay and S. W. M. Kasper, "Efficient $CuInSe_2$/CdS solar cells" *Appl. Phys. Lett.*, vol. 27, 1975.

[22] S. Dieter K, *SEMICONDUCTOR MATERIAL AND DEVICE CHARACTERIZATION*, Third. John Willey and Sons, 2006.

[23] A. M. Gabor, J. R. Tuttle, D. S. Albin, M. A. Contreras, and R. N. M. Hermann, "High-efficiency $CuIn_xGa_{1-x}Se_2$ solar cells made from $(In_x,Ga_{1-x})_2Se_3$ precursor films" *Appl. Phys. Lett.*, vol. 65, no. 2, 1994.
[24] D. Abou-Ras, S. Wagner, B. J. Stanbery, H. W. Schock, R. Scheer, L. Stolt, S. Siebentritt, D. Lincot, C. Eberspacher, K. Kushiya, and A. N. Tiwari, "Innovation highway: Breakthrough milestones and key developments in chalcopyrite photovoltaics from a retrospective viewpoint" *Thin Solid Films*, 2017.
[25] B. J. Stanbery, W. S. Chen, and R. A. Mickelsen, "INTEGRATED THIN-FILM $CuInSe_2$ MONOLITHIC SOLAR CELL MODULES." in *Proceedings - The Electrochemical Society*, 1985, vol. 85–9, pp. 115–121.
[26] G. Sozzi, S. Di, R. Menozzi, B. Bissig, S. Buecheler, and A. N. Tiwari, "Impact of front-side point contact/passivation geometry on thin- film solar cell performance" *Sol. Energy Mater. Sol. Cells*, vol. 165, no. September 2016, pp. 94–102, 2017.
[27] B. Vermang, J. T. Wätjen, V. Fjällström, F. Rostvall, M. Edoff, R. Kotipalli, F. Henry, and D. Flandre, "Employing Si solar cell technology to increase efficiency of ultra-thin $Cu(In,Ga)Se_2$ solar cells" *Prog. Photovoltaics Res. Appl.*, vol. 22, no. 10, pp. 1023–1029, 2014.
[28] T. Dullweber, U. Rau, and H. W. Schock, "A new approach to high-efficiency solar cells by band gap grading in $Cu(In,Ga)Se_2$ chalcopyrite semiconductors" *Sol. energy Mater. Sol. cells*, vol. 67, pp. 145–150, 2001.
[29] B. Vermang, V. Fjallström, X. Gao, and M. Edoff, "Improved rear surface passivation of $Cu(In,Ga)Se_2$ solar cells: A combination of an Al_2O_3 rear surface passivation layer and nanosized local rear point contacts" *IEEE J. Photovoltaics*, vol. 4, no. 1, pp. 486–492, 2014.
[30] J. H. Werner, J. Mattheis, and U. Rau, "Efficiency limitations of polycrystalline thin film solar cells: case of $Cu(In,Ga)Se_2$" *Thin Solid Films*, vol. 480–481, pp. 399–409, Jun. 2005.
[31] P. Casper, R. Hünig, G. Gomard, O. Kiowski, C. Reitz, U. Lemmer, M. Powalla, and M. Hetterich, "Optoelectrical improvement of ultra-thin $Cu(In,Ga)Se_2$ solar cells through microstructured MgF_2 and Al_2O_3 back contact passivation layer" *Phys. Status Solidi - Rapid Res. Lett.*, vol. 10, no. 5, pp. 376–380, 2016.
[32] D. K. Simon, P. M. Jordan, I. Dirnstorfer, F. Benner, C. Richter, and T. Mikolajick, "Symmetrical Al_2O_3-based passivation layers for p- and n-type silicon" *Sol. Energy Mater. Sol. Cells*, vol. 131, pp. 72–76, 2014.
[33] J. Schmidt, A. Merkle, R. Brendel, B. Hoex, M. C. M. van de Sanden, and W. M. M. Kessels, "Surface passivation of high-efficiency silicon solar cells by atomic-layer-deposited Al_2O_3" *Prog. Photovoltaics Res. Appl.*, vol. 16, no. 6, pp. 461–466, Sep. 2008.
[34] W. Wu, Y. Cao, J. V. Caspar, Q. Guo, L. K. Johnson, R. S. McLean, I. Malajovich, and K. R. Choudhury, "Characterization of CZTSSe photovoltaic device with an atomic layer-deposited passivation layer" *Appl. Phys. Lett.*, vol. 105, no. 4, 2014.
[35] Y. Fu, N. A. Allsop, S. E. Gledhill, T. Köhler, M. Krüger, R. Sáez-Araoz, U. Blöck, M. C. Lux-Steiner, and C. H. Fischer, "ZnS nanodot film as defect passivation layer for $Cu(In,Ga)(S,Se)_2$ thin-film solar cells deposited by Spray-ILGAR (ion-layer gas reaction)" *Adv. Energy Mater.*, vol. 1, no. 4, pp. 561–564, 2011.
[36] A. Bercegol, B. Chacko, R. Klenk, I. Lauermann, M. C. Lux-Steiner, and M. Liero, "Point contacts at the copper-indium-gallium-selenide interface - A theoretical outlook" *J. Appl. Phys.*, vol. 119, no. 15, 2016.
[37] R. Ratan Kotipalli, "Surface Passivation Effects of Aluminum Oxide on Ultra-Thin CIGS Solar Cells" Ecole Polytechnique De Louvain, 2016.
[38] K. Piskorski and H. M. Przewlocki, "The methods to determine flat-band voltage V_{fb} in semiconductor of a MOS structure" *MIPRO, 2010 Proc. 33rd Int. Conv.*, 2010.
[39] E. H. Nicollian and J. R. Brews, *MOS (metal oxide semiconductor) physics and technology*. 1982.
[40] S. M. Sze and K. K. Ng, *Physics of Semiconductor Devices*. Hoboken, NJ, USA: John Wiley & Sons, Inc., 2006.

[41] R. Kotipalli, B. Vermang, J. Joel, R. Rajkumar, M. Edoff, and D. Flandre, “Investigating the electronic properties of Al_2O_3/Cu(In,Ga)Se_2 interface” *AIP Adv.*, vol. 5, no. 10, pp. 0–6, 2015.

[42] R. Naciri, H. Bihri, A. Mzerd, A. Rahioui, M. Abd-Lefdil, and C. Messaoudi, *The role of the CdS buffer layer in the $CuInS_2$ Thin film solar cell*. 2007.

[43] D. Regesch, L. Gütay, J. K. Larsen, V. Deprédurand, D. Tanaka, Y. Aida, and S. Siebentritt, “Degradation and passivation of $CuInSe_2$” *Appl. Phys. Lett.*, vol. 101, no. 11, p. 112108, Sep. 2012.

[44] J. Lindahl, U. Zimmermann, P. Szaniawski, T. Torndahl, A. Hultqvist, P. Salomé, C. Platzer-Björkman, and M. Edoff, “Inline Cu(In,Ga)Se_2 co-evaporation for high-efficiency solar cells and modules” *IEEE J. Photovoltaics*, vol. 3, no. 3, pp. 1100–1105, 2013.

[45] D. Liao and A. Rockett, “Cd doping at the $CuInSe_2$/CdS heterojunction” *J. Appl. Phys.*, vol. 93, no. 11, pp. 9380–9382, Jun. 2003.

[46] J. Wang, J. Zhu, and Y. X. He, “The influence of different locations of sputter guns on the morphological and structural properties of Cu–In–Ga precursors and Cu(In,Ga)Se_2 thin films” *Appl. Surf. Sci.*, vol. 288, pp. 109–114, Jan. 2014.

[47] S. Roy, P. Guha, S. N. Kundu, H. Hanzawa, S. Chaudhuri, and A. K. Pal, “Characterization of Cu(In,Ga)Se_2 films by Raman scattering” *Mater. Chem. Phys.*, vol. 73, no. 1, pp. 24–30, Jan. 2002.

[48] K. K. Nanda, S. N. Sarangi, S. N. Sahu, S. K. Deb, and S. N. Behera, “Raman spectroscopy of CdS nanocrystalline semiconductors” *Phys. B Condens. Matter*, vol. 262, no. 1–2, pp. 31–39, Feb. 1999.

[49] J. Bi, L. Yao, J. Ao, S. Gao, G. Sun, Q. He, Z. Zhou, Y. Sun, and Y. Zhang, “Pulse electro-deposition of copper on molybdenum for Cu(In,Ga)Se_2 and $Cu_2ZnSnSe_4$ solar cell applications” *J. Power Sources*, vol. 326, pp. 211–219, Sep. 2016.

[50] M. Sugiyama, H. Sakakura, S.-W. Chang, and M. Itagaki, “Investigation of Sputtering Damage around pn Interfaces of Cu(In,Ga)Se_2 Solar Cells by Impedance Spectroscopy” *Electrochim. Acta*, vol. 131, pp. 236–239, Jun. 2014.

[51] Y. S. Lee, T. Gershon, T. K. Todorov, W. Wang, M. T. Winkler, M. Hopstaken, O. Gunawan, and J. Kim, “Atomic Layer Deposited Aluminum Oxide for Interface Passivation of $Cu_2ZnSn(S,Se)_4$ Thin-Film Solar Cells” *Adv. Energy Mater.*, vol. 6, no. 12, p. 1600198, Jun. 2016.

[52] W.-W. Hsu, J. Y. Chen, T.-H. Cheng, S. C. Lu, W.-S. Ho, Y.-Y. Chen, Y.-J. Chien, and C. W. Liu, “Surface passivation of Cu(In,Ga)Se_2 using atomic layer deposited Al_2O_3” *Appl. Phys. Lett.*, vol. 100, no. 2, p. 23508, 2012.

[53] B. Li, Y. Xie, J. Huang, and Y. Qian, “Synthesis by a Solvothermal Route and Characterization of $CuInSe_2$ Nanowhiskers and Nanoparticles” *Adv. Mater.*, vol. 11, no. 17, pp. 1456–1459, 1999.

[54] P. M. P. Salome, J. P. Teixeira, J. Keller, T. Torndahl, S. Sadewasser, and J. P. Leitao, “Influence of CdS and ZnSnO Buffer Layers on the Photoluminescence of Cu(In,Ga)Se_2 Thin Films” *IEEE J. Photovoltaics*, vol. 7, no. 2, pp. 670–675, Mar. 2017.

[55] J. P. Teixeira, R. A. Sousa, M. G. Sousa, A. F. da Cunha, P. A. Fernandes, P. M. P. Salomé, and J. P. Leitão, “Radiative transitions in highly doped and compensated chalcopyrites and kesterites: The case of Cu_2ZnSnS_4” *Phys. Rev. B*, vol. 90, no. 23, p. 235202, Dec. 2014.

[56] S. Shimakawa, K. Kitani, S. Hayashi, T. Satoh, Y. Hashimoto, Y. Takahashi, and T. Negami, “Characterization of Cu(In,Ga)Se_2 thin films by time-resolved photoluminescence” *Phys. status solidi*, vol. 203, no. 11, pp. 2630–2633, Sep. 2006.

[57] W. K. Metzger, I. L. Repins, M. Romero, P. Dippo, M. Contreras, R. Noufi, and D. Levi, “Recombination kinetics and stability in polycrystalline Cu(In,Ga)Se_2 solar cells” *Thin Solid Films*, vol. 517, no. 7, pp. 2360–2364, Feb. 2009.

[58] G. Friesen, M. . Özsar, and E. . Dunlop, “Impedance model for CdTe solar cells exhibiting constant phase element behaviour” *Thin Solid Films*, vol. 361–362, pp. 303–308, Feb. 2000.

[59] R. Kotipalli, O. Poncelet, G. Li, Y. Zeng, L. A. Francis, B. Vermang, and D. Flandre, “Addressing the impact of rear surface passivation mechanisms on ultra-thin Cu(In,Ga)Se_2 solar

cell performances using SCAPS 1-D model" *Sol. Energy*, vol. 157, pp. 603–613, Nov. 2017.

6 Annexes

6.1. Annex A – Raman spectra

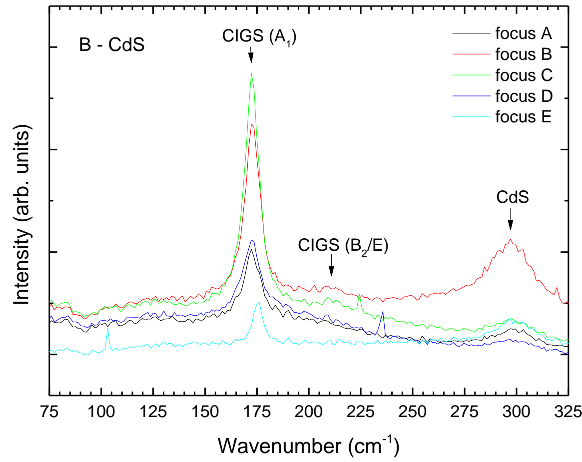

a)

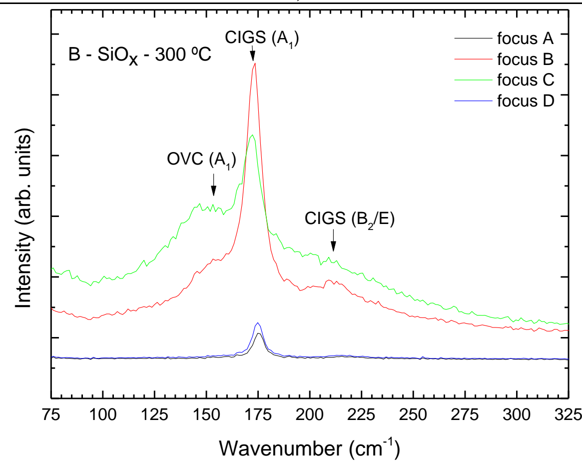

b)

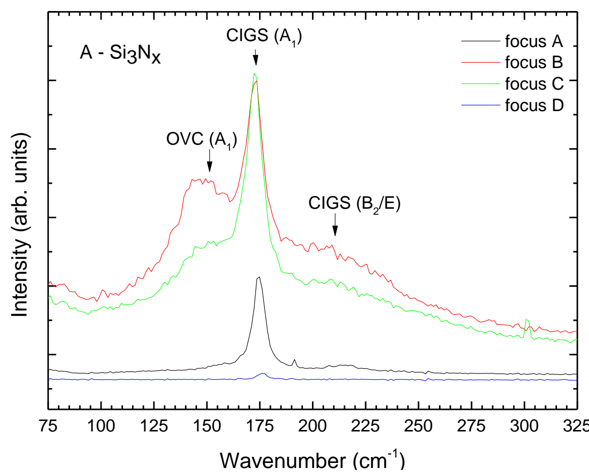

c)

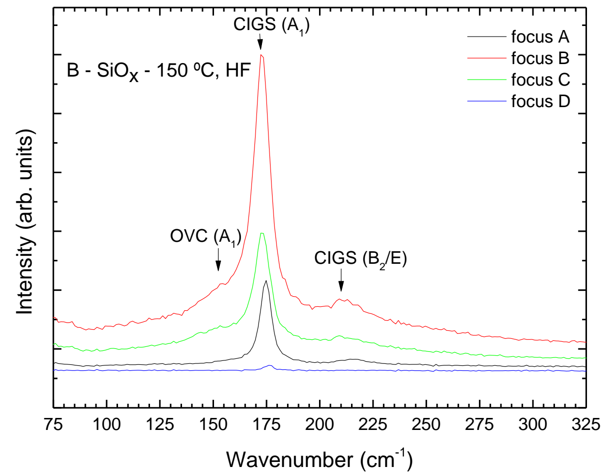

d)

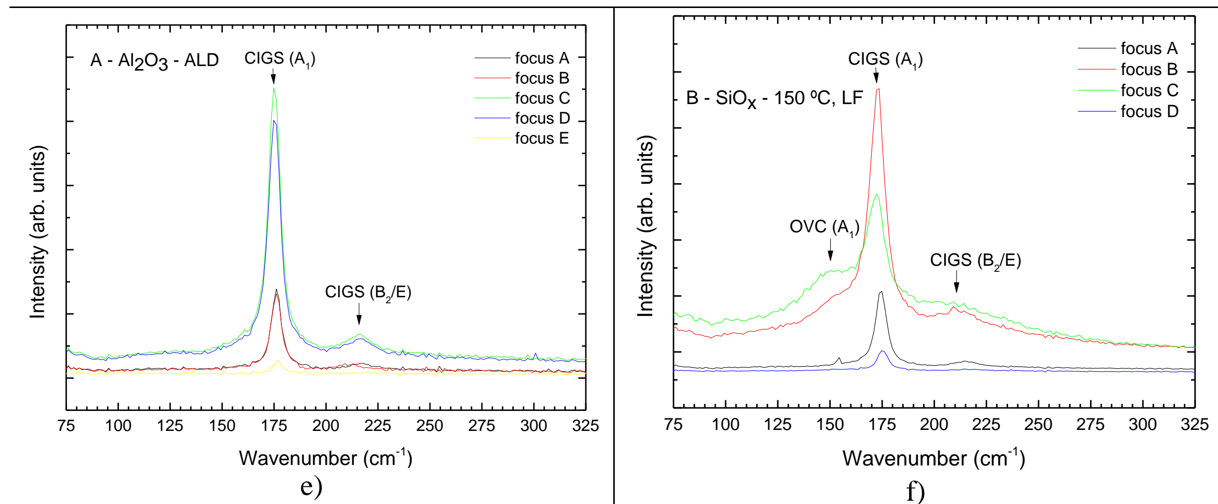

Figure 6.1 Raman spectra with different focus point of CIGS A in the left side and CIGS B in the right side. Each graph represents: a) B – CdS; b) B - SiO_x - 300 ºC; c) A - Si_3N_x - 150 ºC, HF; d) B - SiO_x - 150 ºC, HF; e) A - Al_2O_3 - ALD and f) B - SiO_x - 150 ºC, LF. The curves with low peak intensities are out of focus.

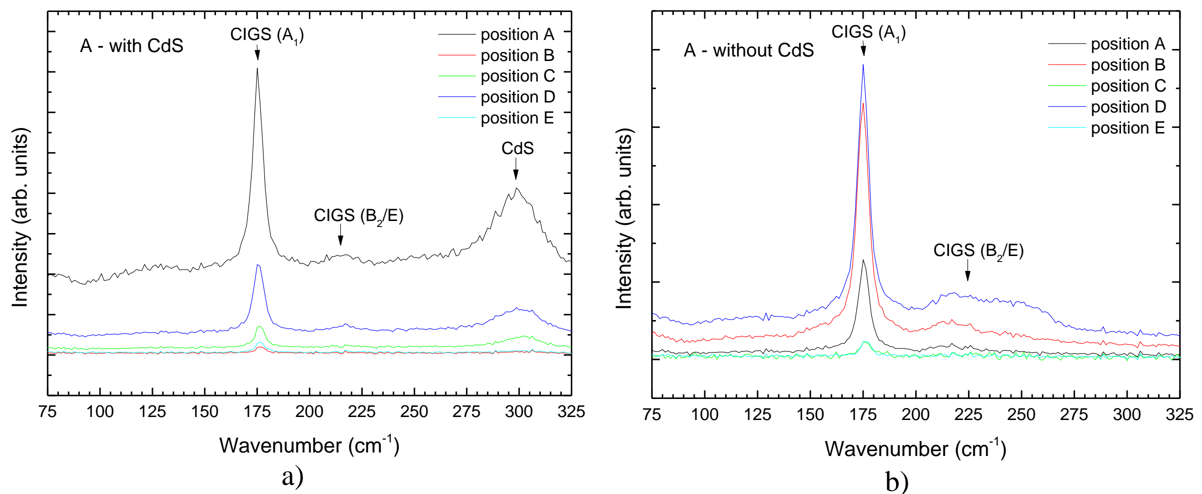

Figure 6.2 Raman spectra of: a) Before CdS removal and b) After CdS removal.

6.2. Annex B – X-ray diffraction spectra

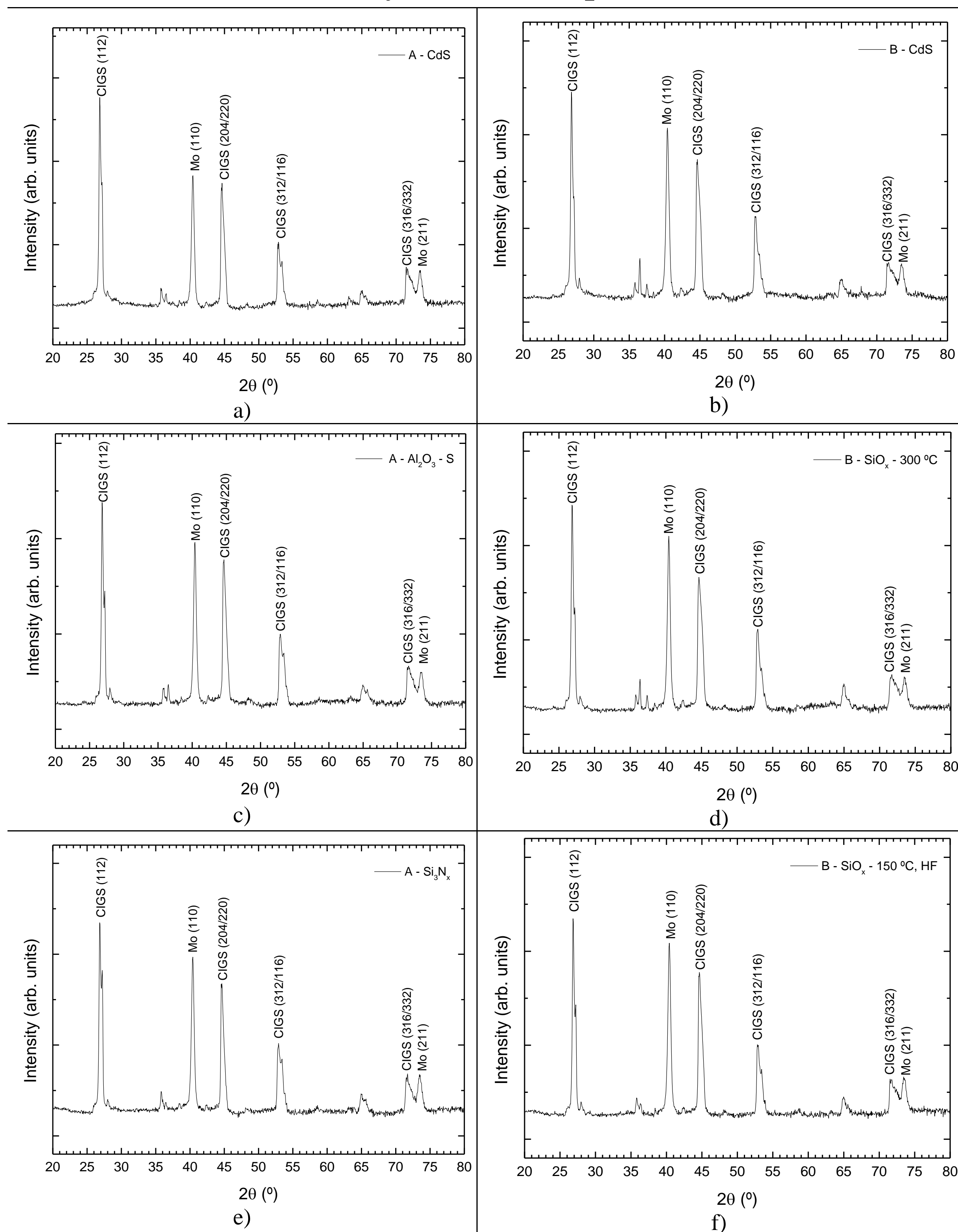

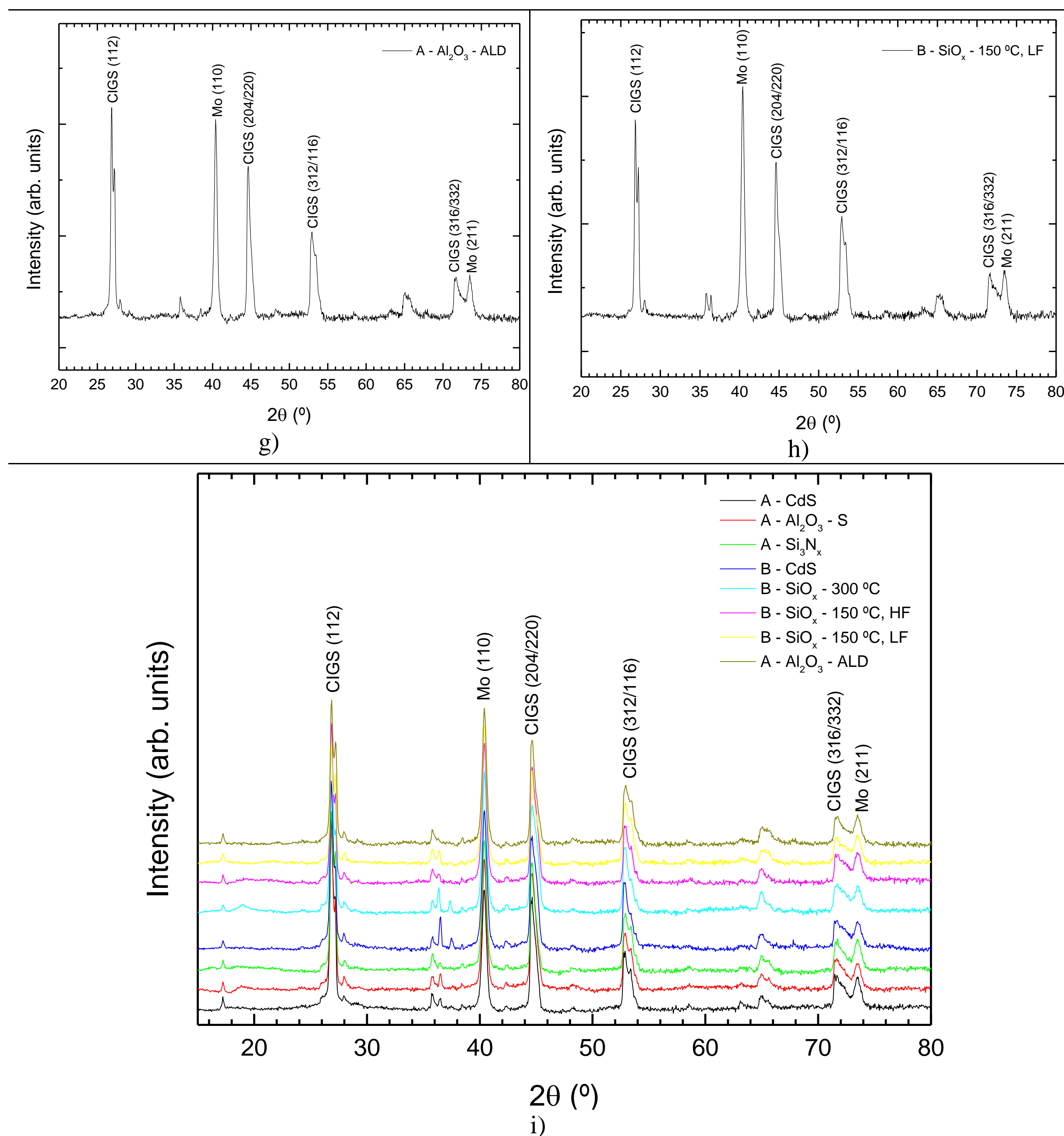

Figure 6.3 X-ray diffraction spectra of: a) A - CdS; b) B - CdS; c) A - Al_2O_3 - S; d) B - SiO_x - 300 ºC; e) A - Si_3N_x; f) B - SiO_x - 150 ºC, HF; g) A - Al_2O_3 - ALD; h) B - SiO_x - 150 ºC, LF and i) all samples together.

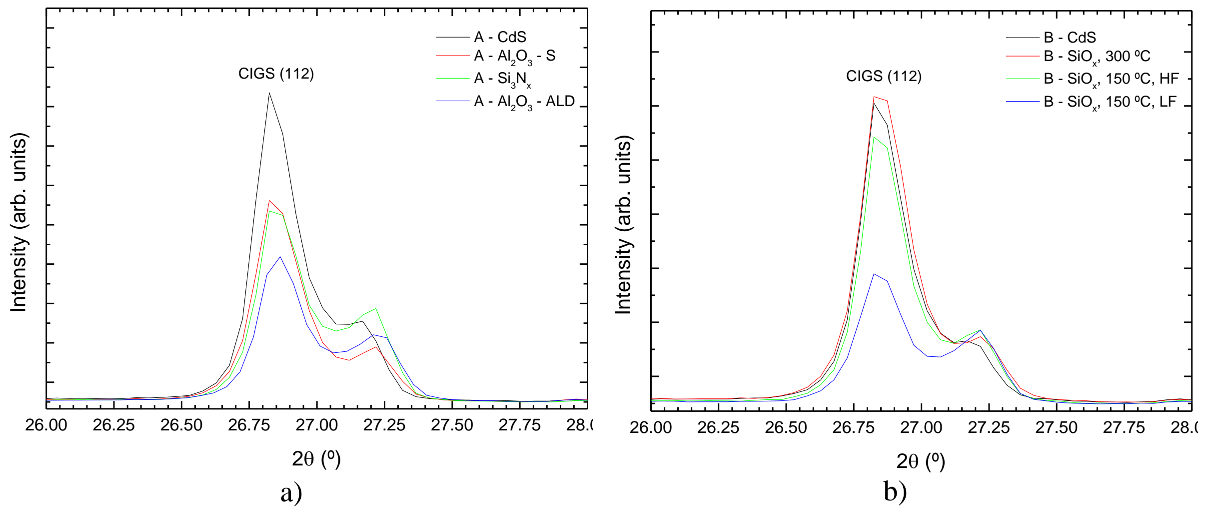

Figure 6.4 - X-ray diffraction spectra zoom of the main CIGS peak (112). a) A - CdS, A - Al_2O_3 - S, A - Si_3N_x and A - Al_2O_3 – ALD samples; b) B - CdS, B - SiO_x - 300 ºC, B - SiO_x - 150 ºC, HF and B - SiO_x - 150 ºC, LF samples.

6.3. Annex C – Fixed insulator charges (Q_f) and Density of interface defects (D_{it})

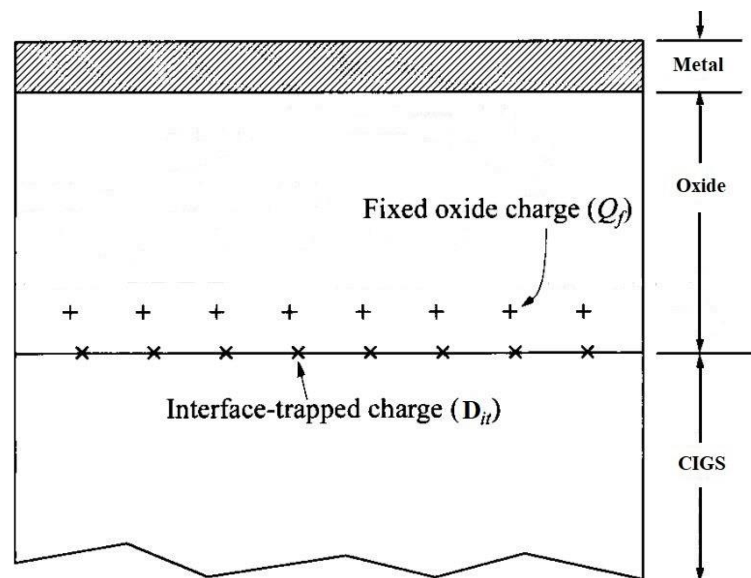

Figure 6.5 - Location of the fixed insulator charges (example of positive charges) and the density of interface defects in the CIGS/insulator interface. Adapted from [40].

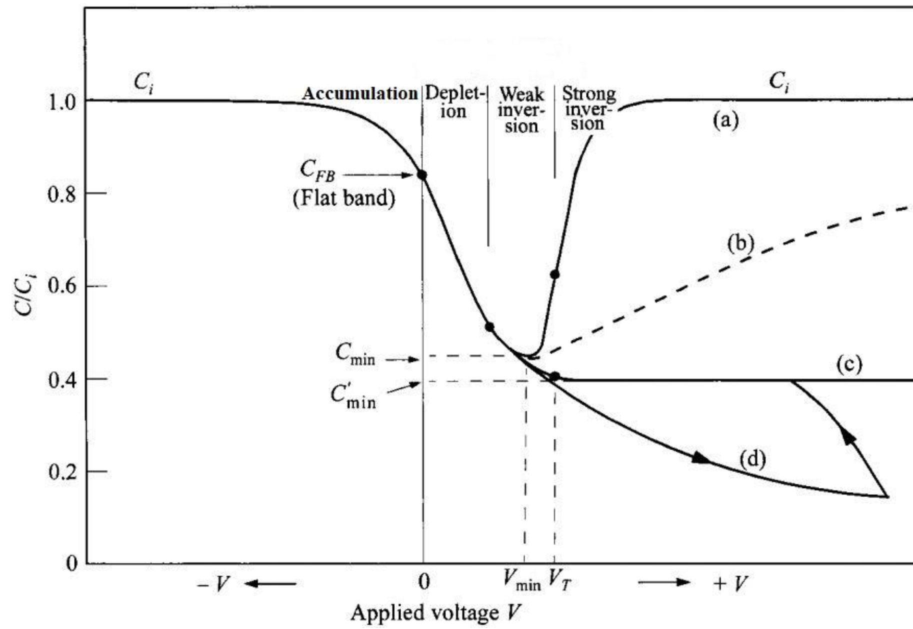

Figure 6.6 - Ideal MIS C-V curves of a p-type semiconductor: (a) Low frequency; (b) Intermediate frequency; (c) High frequency; (d) High freequency with fast-sweep (deep depletion). Flat-band voltage of 0V is assumed. Adapted from [40].

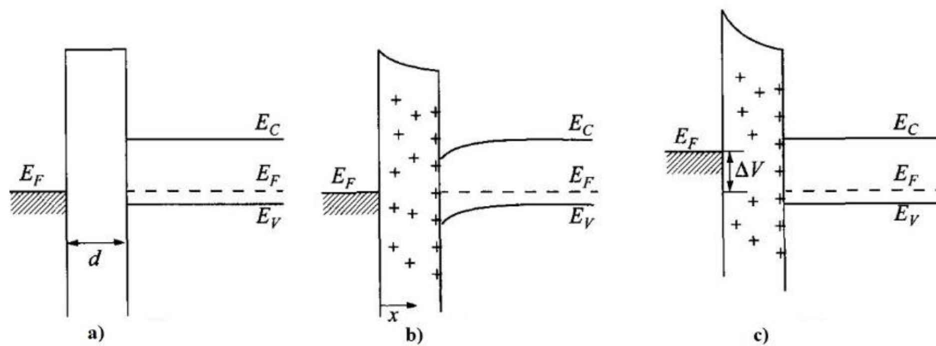

Figure 6.7 - Band diagram of a MIS with a p-type semiconductor. a) Ideal MIS in flat-band; b) MIS with positive insulator charges and band bending; c) New flat-band bias. Adapted from [40].